Local Generation of Mirror Modes by Pickup Protons at Mars

C. Simon Wedlund, C. Mazelle, K. Meziane, C. Bertucci, M. Volwerk, L. Preisser, D. Schmid, J. Halekas, J. Mcfadden, D. Mitchell, et al.

JGR Space Physics

RESEARCH ARTICLE
10.1029/2024JA033275

Local Generation of Mirror Modes by Pickup Protons at Mars

C. Simon Wedlund[1,2], C. Mazelle[2], K. Meziane[3], C. Bertucci[4], M. Volwerk[1], L. Preisser[5], D. Schmid[1], J. Halekas[6], J. McFadden[7], D. Mitchell[7], J. Espley[8], and P. Henri[5,9]

[1]Space Research Institute, Austrian Academy of Sciences, Graz, Austria, [2]Institut de Recherche en Astrophysique et Planétologie, CNRS, University of Toulouse, CNES, Toulouse, France, [3]University of New Brunswick, Fredericton, NB, Canada, [4]IAFE/CONICET, University of Buenos Aires, Ciudad Autónoma de Buenos Aires, Argentina, [5]LPC2E, CNRS, Université d'Orléans, CNES, Orléans, France, [6]Department of Physics and Astronomy, University of Iowa, Iowa City, IA, USA, [7]Space Sciences Laboratory, University of California at Berkeley, Berkeley, CA, USA, [8]NASA Goddard Space Flight Center, Greenbelt, MA, USA, [9]Laboratoire Lagrange, Observatoire de la Côte d'Azur/Université de la Côte d'Azur, Nice, France

Key Points:

- First detection of mirror-mode structures detected in the close vicinity of their generation region at Mars
- Main source of temperature anisotropy identified as unstable pickup proton distributions, as previously seen at comets
- Both quasi-perpendicular shock and pickup ion distributions play a role in the generation of the instability at Mars

Correspondence to:
C. Simon Wedlund,
cyril.simon-wedlund@oeaw.ac.at

Citation:
Simon Wedlund, C., Mazelle, C., Meziane, K., Bertucci, C., Volwerk, M., Preisser, L., et al. (2025). Local generation of mirror modes by pickup protons at Mars. *Journal of Geophysical Research: Space Physics*, *130*, e2024JA033275. https://doi.org/10.1029/2024JA033275

Received 9 SEP 2024
Accepted 17 DEC 2024

Author Contributions:
Conceptualization: C. Simon Wedlund, C. Mazelle, K. Meziane, C. Bertucci
Data curation: C. Simon Wedlund, C. Mazelle, K. Meziane, C. Bertucci, J. Halekas, J. McFadden, D. Mitchell, J. Espley
Formal analysis: C. Simon Wedlund, C. Mazelle, K. Meziane, M. Volwerk, J. Halekas
Funding acquisition: C. Simon Wedlund
Investigation: C. Simon Wedlund, C. Mazelle, K. Meziane
Methodology: C. Simon Wedlund, C. Mazelle, K. Meziane, C. Bertucci, M. Volwerk, J. McFadden, P. Henri
Project administration: C. Simon Wedlund
Resources: C. Simon Wedlund, C. Mazelle
Software: C. Simon Wedlund, M. Volwerk, L. Preisser, D. Schmid
Supervision: C. Simon Wedlund
Validation: C. Simon Wedlund, C. Mazelle, K. Meziane, C. Bertucci,

Abstract Mirror mode structures are born from a plasma instability driven by a large temperature anisotropy and appear downstream of planetary and interplanetary shocks, in their magnetosheath. As so-called "magnetic bottles" imprisoning dense and hot plasma, they are usually observed downstream of their region of formation, where the anisotropy is large and free energy is available, implying that they are advected with the plasma flow to the detection region. At Earth and other planets, the quasi-perpendicular shock provides the plasma with the necessary heating along the perpendicular direction to the local magnetic field. At Mars, which boasts an extended exosphere, an additional source of temperature anisotropy exists, through unstable ring-beam velocity distributions, that is, through ions locally ionized and subsequently picked up by the local electric fields. We report here for the first time an example of near locally-generated mirror mode structures due to pickup protons at Mars using the full plasma instrument suite on board the Mars Atmosphere and Volatile EvolutioN (MAVEN) mission. We present events with mirror modes in quasi-perpendicular and quasi-parallel shock conditions, discuss the locality of their generation and show that, in addition to the classic quasi-perpendicular source of anisotropy, another source exists, that is, unstable pickup protons. The existence at Mars of this extra ion anisotropy-generating mechanism is reminiscent of comets.

1. Introduction

Space plasma instabilities play a major role in the magnetoenvironment of planets and comets and help redistribute the incoming energy of the solar wind (SW) into the magnetospheres, induced or not, of these objects, heating the local plasma via wave-particle and wave-wave interactions (Gary et al., 1993; Matteini et al., 2012).

The mirror mode instability is one such plasma instability: it gives rise to the formation of large structures, several tens of SW proton Larmor radii in size (or a good fraction of a planetary radius), called mirror modes (MiMos), which are present downstream of planetary and interplanetary shocks, that is, the magnetosheath. These structures are long-wavelength, linearly polarized wave modes that are stationary with respect to the plasma rest frame (e.g., Tsurutani, Lakhina, et al., 2011). They are observed in the spacecraft rest frame in the ultra-low frequency (ULF) range, most often in the shape of trains of peaks or dips in the magnetic field (e.g., Gary, 1992; Génot, 2008; Joy et al., 2006; Soucek et al., 2008). MiMos have the magnetic topology of so-called magnetic bottles confining hot and dense ions and electrons in their midst (Horbury & Lucek, 2009) and which are drifting, mostly unchanged, with the ambient plasma flow (Kivelson & Southwood, 1996; Russell et al., 2008).

The mirror mode instability is driven by a large temperature anisotropy which gives the necessary free energy for the kinetic instability to grow. It competes in such an anisotropic plasma with the electromagnetic ion cyclotron (EMIC) mode, with the ion plasma beta β_i as the main arbiter. For low β values, EMIC dominates over MiMos, whereas for higher β values, the reverse holds (Gary, 1992). However, a minute addition of heavier ions such as He^{2+} (naturally present in the SW in the range of 4%–8% of the SW proton density) or O^+ and O_2^+ as observed at Mars, the EMIC instability is damped and MiMos dominate (Gary, 1992; Price et al., 1986), which explains the widespread occurrence of MiMos in the Earth's magnetosheath (e.g., Tsurutani, Lakhina, et al., 2011). The

J. Halekas, J. McFadden, D. Mitchell, J. Espley
Visualization: C. Simon Wedlund
Writing – original draft: C. Simon Wedlund, C. Mazelle, K. Meziane, C. Bertucci, M. Volwerk
Writing – review & editing: C. Simon Wedlund, C. Mazelle, K. Meziane, C. Bertucci, M. Volwerk, L. Preisser, D. Schmid, J. Halekas, J. McFadden, D. Mitchell, J. Espley, P. Henri

instability typically grows when the mirror mode instability criterion (MMIC) is fulfilled (Califano et al., 2008; Chandrasekhar et al., 1958; Ferrière & André, 2002; Gary, 1992; Génot et al., 2001, 2009; Hasegawa, 1969; Hellinger, 2007; Pokhotelov et al., 2001, 2004; Price, 1989; Vedenov & Sagdeev, 1961):

$$\mathrm{MMIC} = 1 + \sum_j \beta_{\perp,j}\left(1 - \frac{\beta_{\perp,j}}{\beta_{\parallel,j}}\right) < 0 \tag{1}$$

where all species j (electrons and ions) contribute to the overall anisotropy of the plasma, with $\perp$ and $\parallel$ denoting the perpendicular and parallel directions to the background magnetic field direction. Soucek et al. (2008) and Balikhin et al. (2009) also showed that inside a MiMo structure the plasma is in pressure balance and unstable to the generation of MiMos in a dip structure, whereas outside of the structure, the plasma is marginally stable, reinforcing the idea of a magnetic bottle trapping dense and hot plasma advected downstream with the plasma, as confirmed with Cluster observations (Horbury & Lucek, 2009; Soucek & Escoubet, 2011). Another characteristic of the MiMo structure is an antiphase between the total magnetic field intensity $|\mathbf{B}|$ and the plasma density N_j modulated by the temperature anisotropy $T_\perp/T_\parallel$, so that perturbations in plasma density and magnetic field take the form (Hasegawa, 1969):

$$\frac{\Delta N_j}{N_j} = \left(1 - \frac{T_{\perp,j}}{T_{\parallel,j}}\right)\frac{\Delta B_\parallel}{B}. \tag{2}$$

the source of this kinetic temperature anisotropy is manifold. One source arises from the so-called quasi-perpendicular (Q-$\perp$) shock, where the geometry of the shock is defined by the angle, noted θ_{Bn} , between the impinging SW magnetic field direction and the local normal to the shock surface. Immediately downstream of it, a Q-$\perp$ shock ($\theta_{Bn} \gtrsim 45°$) provides the plasma with a preferential heating along the perpendicular direction to the local magnetic field, a free energy that is conducive to the generation of MiMos (Burgess & Scholer, 2015). This source of anisotropy is present at all planets of the solar system, including Earth, for which the Q-$\perp$ shock is the main source of the anisotropy, and Mars (Simon Wedlund, Volwerk, Mazelle, et al., 2022). In this scenario, MiMos start growing immediately downstream of the shock but are detected far downstream of it, close to the magnetic pileup boundary (MPB), where they start piling up (Simon Wedlund et al., 2023). Downstream of a quasi-parallel (Q-$\parallel$ shock, $\theta_{Bn} \lesssim 45°$), no such temperature anisotropy is expected to arise and no MiMos are usually excited, although a plethora of ULF waves are still present upstream, in the foreshock region (Burgess et al., 2005).

In contrast to the Earth, Mars boasts an extended exosphere, in a manner similar to comets, or to certain moons of gas giants. In this case, another source of temperature anisotropy theoretically exists: unstable pickup ion distributions, in the shape of ring-beam velocity distribution functions (VDFs) in the plasma rest frame (Price, 1989; Szegö et al., 2000). In general, such a VDF is characterized by a beam component along the field and a perpendicular component associated with the gyromotion around the magnetic field **B**, the relative value of both components depending only on the local cone angle between the **B**-field and the bulk plasma velocity vector, noted α_{BV}, at the location of the original neutral ionisation. In this case, the instability arises mostly from the velocity drift between SW and newly picked up ions $(\alpha_{BV} \sim 0°)$. However, for a large-enough cone angle $(\alpha_{BV} \sim 90°)$, the ring component of the distribution results in ion temperatures $T_\perp > T_\parallel$, itself another potential source of free energy for microinstabilities (Gary, 1992; Gary et al., 1993). This mechanism is particularly efficient at comets, which are a prime example of a spatially extended neutral atmosphere (Brinca & Romeiras, 1998; Glassmeier et al., 1993; Mazelle et al., 1991; Tsurutani & Smith, 1986). Because the exosphere of these objects pervades their entire magnetoenvironments, from the SW upstream of the shock to the magnetosheath downstream of it, this extra source of anisotropy is expected everywhere (see Simon Wedlund et al., 2023). At Mars, it is most likely modulated by atmospheric and exospheric seasons, with the hydrogen exosphere providing the bulk of the magnetosheath pickup ions in the form of pickup protons (Halekas, 2017). Besides that expected at Mars and observed at comets, wave generation through unstable pickup ion distributions has also been observed around the moons of Jupiter, especially at Io (Huddleston et al., 2000; Russell et al., 1999).

To this date and to the authors' knowledge, the pickup ion source of anisotropy for the generation of mirror modes has, however, never been studied at Mars, Venus or comets with a full plasma suite. The NASA/Mars Atmosphere

and Volatile EvolutioN (MAVEN) mission (Jakosky et al., 2015), embarking both in situ ion and electron instruments for the first time at Mars (Halekas et al., 2015; McFadden et al., 2015; Mitchell et al., 2016), remedies this lack. These instruments' temporal resolutions of 2–8 s are perfect to characterize structures whose durations are on average about 10–15 s.

At Mars, mirror modes have first been noted in Mars Global Surveyor (MGS) data (Bertucci et al., 2004), but no definite proof was possible until MAVEN was in orbit (Simon Wedlund, Volwerk, Mazelle, et al., 2022). Two statistical studies of the occurrence of mirror-mode-like waves followed (Jin et al., 2022; Simon Wedlund et al., 2023), showing that these structures tend to concentrate in two main regions at Mars, one close to the MPB for medium-to-low solar zenith angles, the other immediately downstream of the bow shock for high solar zenith angles. Besides anisotropy-driven instabilities, the Martian environment contains a wealth of ULF waves excited upstream and downstream of the shock (Espley et al., 2004; Mazelle et al., 2004; Romanelli et al., 2016; Romeo et al., 2021; Ruhunusiri et al., 2015) as well as SW transients (e.g., Madanian et al., 2020). A current topic of importance in the Mars community is the possible transmission and effectiveness (in a way similar to the geoeffectiveness at Earth) of such phenomena into the inner magnetoenvironment, which has recently been investigated with observations and numerical simulations (Collinson et al., 2018; Fowler et al., 2018; Jarvinen et al., 2022).

We present here for the first time at Mars observations of locally generated MiMo structures, that is, structures detected in the vicinity of their generation region. We identify the free energy source as coming from unstable pickup proton distributions. Using MAVEN plasma and magnetic field instruments (Section 2), we compare in Section 3 two main cases of clear trains of MiMos in the subsolar magnetosheath when the Martian exosphere is at its largest extension, one in a Q-⊥ shock condition, where the temperature anisotropy grows immediately downstream of the shock, the other in a Q-|| shock configuration, where the latter mechanism is minimized. In Section 4, we discuss the local generation of the instability through pickup protons, emphasizing that Mars, like comets but unlike Earth, has many sources of anisotropy that act together to generate the instability.

2. Methodology

2.1. Instrumentation

MAVEN is a tri-axis stabilized spacecraft with a period of about 4 hr, probing the Martian magneto-environment, from the SW to the inner magnetosphere and ionosphere, including the magnetosheath (Jakosky et al., 2015). For this study, we use three main instruments: MAG, SWIA, SWEA, and one supporting instrument, STATIC.

MAG is the magnetometer on board MAVEN (Connerney, Espley, Lawton et al., 2015), sampling at 32-Hz the magnetic field vector and intensity with an accuracy better than 0.05%. Because MiMos have typical durations of a few seconds to tens of seconds, the **B**-field is downsampled to 1 Hz in the following.

SWIA, the SW Ion Analyzer (Halekas et al., 2015), captures the total ion differential flux per energy bin (within a range in energy per charge of 5×10^{-3}–25 keV/q) in several scanning-telemetry modes (Halekas, Brain et al., 2017). SWICA (Coarse Archive mode), with a field of view (FOV) of 360° × 90° ($\Delta\phi = \Delta\theta = 22.5°$) and a resolution of 8–16 s is the preferred mode in the magnetosheath where ions have a broad angular VDF. SWIFA (Fine Archive mode) has a smaller FOV (45° × 45°, $\Delta\phi = \Delta\theta = 4.5°$) but better temporal resolution (4 s), ideal for the SW upstream of the shock.

STATIC, the Suprathermal and Thermal Ion Composition analyzer, is an ion mass spectrometer (McFadden et al., 2015) with a temporal resolution of 4 s, an energy range of 10^{-4}–30 keV/q and a FOV similar to the SWICA mode of SWIA. It is used here as a supporting instrument to determine which species dominates in the SW and in the magnetosheath.

SWEA, the SW Electron Analyzer (Mitchell et al., 2016), measures the electron differential flux at a maximum cadence of 2 s in the 3–4,600 eV range, over a 360° × 120° FOV. Electron densities at 2–8 s resolution are derived from the omnidirectional energy spectrum. Here, we are interested only in their variations ($\Delta N_e/N_e$), not their absolute values which can often differ from the total ion densities calculated from SWIA and STATIC, due to spacecraft potential and artificial secondary electrons produced in the instrument, especially when fluxes around 100 eV are large, which is the case in the magnetosheath (Andreone et al., 2022). When a constant 2-s

Table 1
Selected Events With MiMo-Like Candidates. θ_{Bn} is the Estimated Angle Between the Normal of the Shock and the IMF Direction. α_{BV} is the Angle Between the IMF Direction and the Solar Wind Proton Bulk Flow Direction

Parameters	Units	Event 1 2016-12-25 20:30–21:20 UT	Event 2 2016-12-26 05:40–06:30 UT	Event 3 2015-09-25 07:55–08:55 UT
Ls	deg	287	287	46
θ_{Bn}[a]	deg	80	27	85
α_{BV}^{sw}	deg	98	156	53
$\lvert\mathbf{B}_{sw}\rvert$	nT	1.5	3.7	2.6
N_{sw}	cm^{-3}	4.3	9.3	1.2
$\lvert\mathbf{V}_{sw}\rvert$	km s^{-1}	306	319	539
SZA'_{shock}[b,c]	deg	7.1	2.6	17.5
SZA'_{MPB}[b,d]	deg	16.5	37.6	22.3
Crossing[e]	–	MSh → SW	MSh → SW	SW → MSh
Remote generation[f]	–	Yes	No	Yes
Local pickup generation[f]	–	Strong	Strong	Weak

Note. The aberrated solar wind zenith angles (SZA'), obtained from a rotation about 4° around the Z_{MSO} axis to compensate for the solar wind velocity aberration with respect to the orbital speed of Mars (Slavin & Holzer, 1981), are given at the approximate time (±60 s) of shock and MPB crossings. All solar wind quantities were derived from the SWIFA mode of MAVEN/SWIA for a chosen interval upstream of major shock's disturbances, typically about 15 min prior to the shock crossing and assuming all ions were protons. [a]θ_{Bn} geometrically derived with an uncertainty of ±5°, from a sample region upstream of the shock. [b]$\tan SZA' = \sqrt{Y'^2_{MSO} + Z^2_{MSO}}/X'_{MSO}$. [c]$t_{shock}$ = 20:52:30 UT (Event 1), t_{shock} = 05:59:30 UT (Event 2), t_{shock} = 08:32:00 UT (Event 3). [d]t_{MPB} = 20:40:55 UT (Event 1), t_{MPB} = 05:45:20 UT (Event 2), t_{MPB} = 08:48:00 UT (Event 3). [e]SW, solar wind; MSh, magnetosheath. [f]Theoretical expectations.

resolution is needed, electron flux variations at an energy of about 100 eV are a useful proxy of the density variations.

In the following, all vector and tensor quantities are expressed in the Mars Solar Orbital (MSO) coordinate system. From the center of Mars, X is toward the Sun, Z points toward the North pole, and Y completes the system so that Mars' orbital plane around the Sun is contained in the X–Y plane.

2.2. Event Selection

Two main temperature anisotropy-generating sources theoretically exist at Mars, namely the Q-⊥ bow shock (Simon Wedlund, Volwerk, Mazelle, et al., 2022) and the presence of unstable pickup ion distributions. Using the detection method of Simon Wedlund et al. (2023) to list all potential MiMo-like structures between October 2014 and February 2021, we selected two main events containing MiMo-candidate detections and illustrating these two mechanisms. The hydrogen exosphere of Mars varies widely during a full Martian orbit around the Sun, with Mars' eccentricity playing a major role. We use the solar longitude Ls as a proxy of Mars' exosphere "seasonal" variability with Ls = 270° ± 45° denoting when the exosphere is at its maximum extent (i.e., Northern hemisphere winter solstice), and Ls = 90° ± 45° when the exosphere shrinks to its minimum size (i.e., around the Northern hemisphere summer solstice, Halekas, 2017; Halekas & McFadden, 2021; Yamauchi et al., 2015). When the exosphere is at its maximum extent and pickup ions are expected to play an important role, we choose a pair of (Q-⊥, Q-||) magnetosheath events (labeled Events 1 and 2 in the following). Additionally, we include a typical Q-⊥ event (labeled Event 3), at Ls ∼46° (close to aphelion conditions), when pickup ion effects are expected to contribute much less to the generation of the temperature anisotropy.

Table 1 summarizes their characteristics. Each event takes place in the subsolar magnetosheath: this is to minimize the global size of the magnetosheath probed by the spacecraft, so that MiMo structures do not have time to evolve much from their generation region down to the region of detection. Additionally, the plasma flow in this region is more radial (along the direction of the $-X'_{MSO}$ axis) from the shock to the MPB. The "SW zenith angle,"

SZA′, defined as the angle at the spacecraft location between the SW aberrated X'_{MSO} axis and the X'_{MSO}–$Y'_{MSO}|Z_{MSO}$ planes $\left(\mathrm{SZA}' = \tan^{-1}\left(\sqrt{Y'^2_{MSO} + Z^2_{MSO}}/X'_{MSO}\right)\right)$ is less than ∼30° for all events. The shock conditions are found using the θ_{Bn} angle calculated from Simon Wedlund, Volwerk, Beth, et al. (2022) between the normal to the local shock at the position of MAVEN's crossing and the IMF direction, considered stable over the range of SZAs covered by the spacecraft during an event.

2.3. Wave Analysis and Mirror Mode Characterization

After an event has been selected for a potential MiMo presence using Simon Wedlund et al. (2023), we aim to ascertain the nature of the waves for a specific magnetosheath environment. For that, we propose a two-step approach updated from the work of Simon Wedlund, Volwerk, Mazelle et al. (2022).

In a first step, we wish to obtain an overview of the wave modes present in the magnetosheath. We calculate dynamic Fast Fourier Transform (FFT) spectra of the detrended magnetic field by first transforming **B** into mean field-aligned coordinates (MFA), where the third axis is the direction of the mean field, and the two transverse components are chosen arbitrarily as two perpendicular axes to the MFA axis. The moving FFT combined 5 harmonics, with 512 points per spectrum (totaling 16 s of continuous data), and a window shift of 64 points (2 s, equivalent to electron density data resolutions). We proceed to calculate the magnetic field covariance matrix in the spacecraft rest frame (Means, 1972; Samson & Olson, 1980), yielding from its diagonal elements the wave power as a function of time and frequency in the perpendicular direction to the magnetic field. From the off-diagonal elements, we obtain the wave polarisation percentage (denoting at which frequency the wave modes are excited), the ellipticity (−1 for left-hand [LH] circularly polarized, 1 for right-hand [RH] circularly polarized and 0 for linearly polarized waves), as well as the polarisation angle to the mean field direction (where 0° denotes a wave vector **k** parallel to the MFA direction, whereas 90° denotes the transverse direction to the MFA direction).

In a second step, we characterize the detected magnetosheath structures and ensure that they are indeed MiMos. We use ion and electron plasma data and calculate the terms of Equation 2 to complement the magnetic field analysis. This is because Hasegawa (1969) not only showed that MiMos obey the instability criterion of Equation 1 but that they, as a consequence, follow the density fluctuation relation of Equation 2. This latter equation systematizes the characteristic MiMo-unstable behavior inside the structure (in a "dip," when |**B**| is smallest) and a B-field variability modulated by the temperature anisotropy in antiphase with density N. A good way to ensure that Equation 2 is fulfilled is to compare each term of the equation, that is, $\Delta B_{\|}/B\left(1 - T_{\perp}/T_{\|}\right)$ and $\Delta N/N$.

To derive these quantities, we use the SWICA mode of SWIA at a temporal resolution of 8 s and calculate the temperature anisotropy $T_{\perp}/T_{\|}$ from the pressure tensor elements, as explained in the appendix of Simon Wedlund, Volwerk, Mazelle et al. (2022). Because SWIA has a restricted FOV, uncertainties on the determination of the $T_{\|}$ and $T_{\perp}$ components arise, and are discussed more precisely in Halekas, Ruhunusiri, et al. (2017), and in Simon Wedlund, Volwerk, Mazelle, et al. (2022) in the case of MiMos. For Events 1–3, since MAVEN was near the subsolar region and SWIA is sun-pointed, the bulk of the distribution was usually well captured by the instrument inside the magnetosheath.

3. Mirror Mode Observations: Context and Characterization

In this section, we present the two main mirror mode events chosen (see Table 1), and show that MiMos can not only be present in the magnetosheath downstream of a Q-⊥ shock (Event 1) but also in that of a Q-|| shock (Event 2). During the two full MAVEN orbits separating them, the upstream SW conditions remained qualitatively similar, with very similar SW bulk speeds, although Event 2 had about twice the SW density and IMF intensity of Event 1. In both events, the spacecraft crossed the induced magnetosphere into the magnetosheath for about 10–15 min in the Southern hemisphere $(Z_{MSO} < 0)$ to finally emerge in the SW.

3.1. Event 1: Q-⊥ Magnetosheath, High Exospheric Season

Figures 1a–1f show for Event 1 the total magnetic field with superimposed regions of B–N phase (red) or antiphase (blue) based on the electron density fluctuations (with phase and antiphase determined by a Pearson correlation coefficient of $|\mathcal{R}| > 1/3$), the ion and electron plasma densities, the B-field cone and clock angles, the bulk ion speed from all SWIA modes and cone angle α_{BV} between **B** and $\mathbf{V}_i$ vectors, and the omnidirectional ion

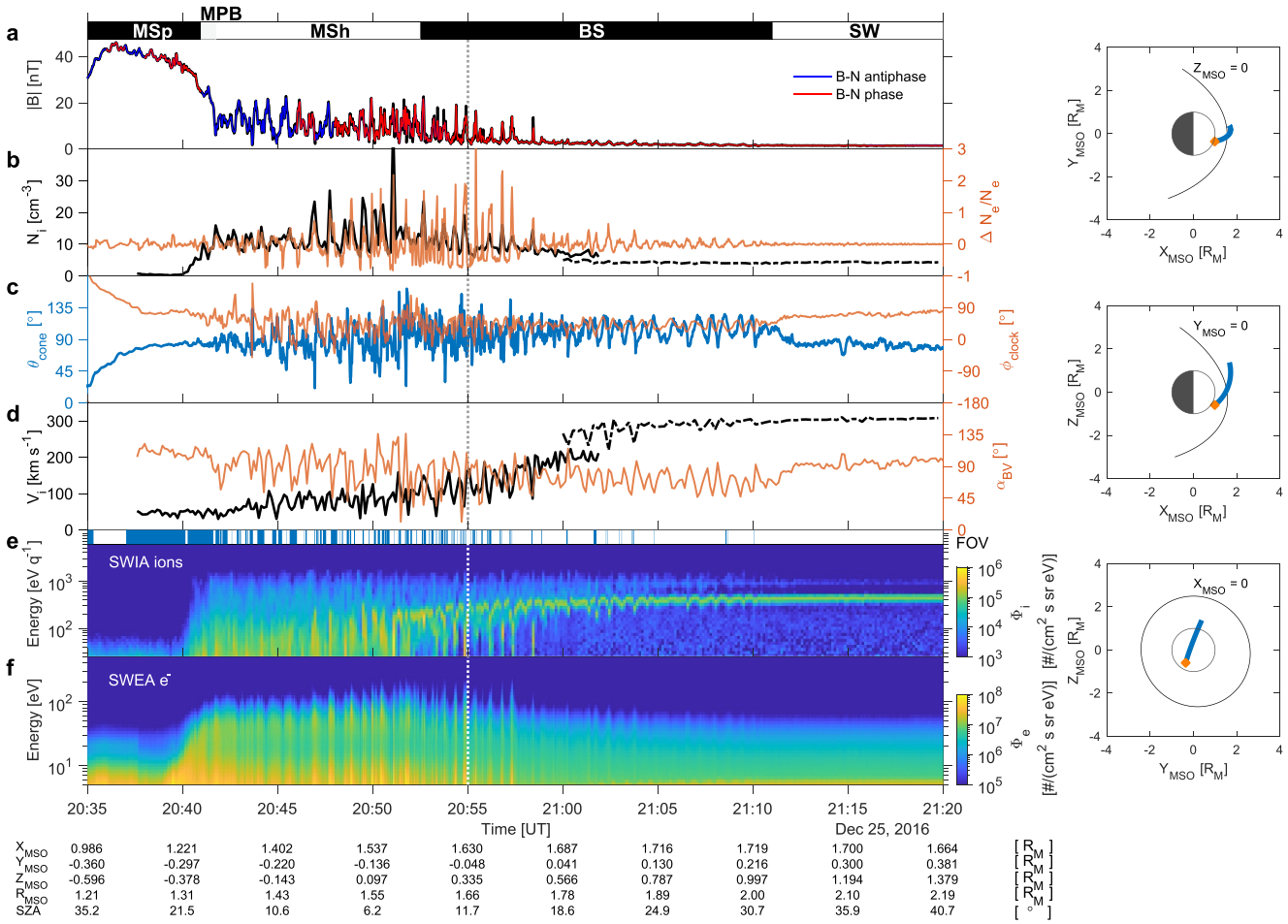

Figure 1. Overview of Event 1 and of the Martian Q-⊥ shock crossing on 25 Dec. 2016 around 21 UT, Ls = 247°. (a) Magnetic field intensity |**B**|. (b) Magnetic field cone and clock angles. (c) Proton density N_i from the SWICA mode (solid black line, left axis) and from the SWIFA mode (dash-dotted black line, left axis), and electron density fluctuations $\Delta N_e/N_e$ (right axis). (d) Ion bulk speed $|\mathbf{V}_i|$ from the SWICA mode (solid black line, left axis) and from the SWIFA mode (dash-dotted black line, left axis) and angle α_{BV} between **B** and $\mathbf{V}_i$ (right axis). (e) Ion omnidirectional flux. (f) Electron omnidirectional flux. In panel (e), top, the field of view information of SWIA is given as a horizontal color bar, with the in-FOV magnetic field in blue and the out-of-FOV magnetic field in white. The dotted vertical line indicates the approximate shock location. Phase and antiphase behavior between |**B**| and N_e in panel (a) was calculated as a moving Pearson correlation coefficient $\mathcal{R}$ with a 60-s window and 30-s overlap. In panel (a), we indicate the most prominent plasma regions: magnetosphere (MSp), magnetic pileup boundary (MPB), magnetosheath (MSh), bow shock region (BS) and solar wind (SW). Panels to the right show MAVEN's orbit during the crossing and its projection unto the X_{MSO}–Y_{MSO}, X_{MSO}–Z_{MSO} and Y_{MSO}–Z_{MSO} planes in units of planetary radius R_M, with the orange cross representing the starting point of the time interval.

and electron fluxes. Cone and clock angles of the magnetic field are defined as $\theta_{\text{cone}} = \arctan\left(\sqrt{B_y^2 + Bz^2}/B_x\right)$ and $\phi_{\text{clock}} = \arctan B_z/B_y$, with $\theta_{\text{cone}} = 0\ [2\pi]$ indicating a sunward [antisunward] magnetic field direction, whereas $\phi_{\text{clock}} = 0\ [\pi/2]$ specifies a field in the $+Y_{\text{MSO}}$ $[+Z_{\text{MSO}}]$ direction. The precise timing at which MAVEN crossed from the magnetosheath into the SW is difficult to ascertain due to the large fluctuations ahead and around of the shock. The approximate position of the shock is shown as a dotted vertical line, following an automatic predictor-corrector algorithm (Simon Wedlund et al., 2021; Simon Wedlund, Volwerk, Beth, et al., 2022). Our best estimate of the outermost boundary of the magnetosheath is at 20:52 UT, when the SW ion beam disappears (Figure 1e). Earlier, the time at which the magnetic field strongly ramped up and the ion and electron fluxes started to decrease in energy defines the start of the MPB and the progressive entering into the induced magnetosphere (around 20:41 UT).

Large-amplitude field and plasma fluctuations were present at about 21:11 UT, when there was a small directional discontinuity (Figure 1c). MAVEN entered the pristine SW after this time as shown in the ion spectra (Figure 1e), when ion flux fluctuations flattened out. This timing is consistent with the width of the ion foot of the Q-⊥ shock,

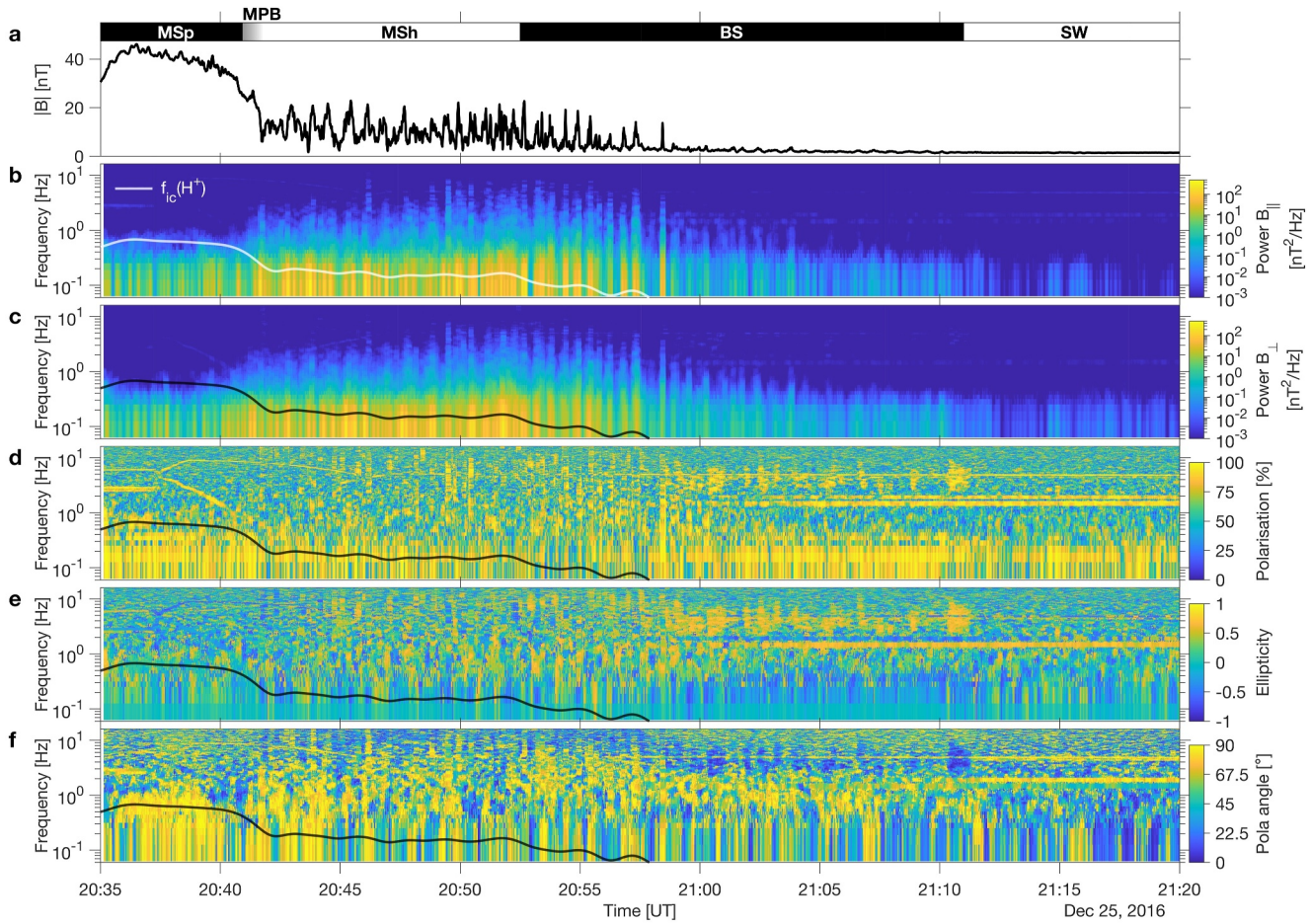

Figure 2. Cross spectral analysis of the 32-Hz **B**-field data in the spacecraft rest frame for Event 1 (Q-⊥ shock, Ls = 287°). (a) Total magnetic field |**B**|. (b, c) Wave power in the $\mathbf{B}_{||}$ and $\mathbf{B}_{\perp}$ directions. (d) Percentage of wave polarisation. (e) Wave ellipticity. (f) Polarisation angle. The local proton gyrofrequency f_{ic} is superimposed as a white or black line.

which was unusually large for this event (about 2,500 km), due to the low value of the SW |**B**| (Gosling & Robson, 1985; Mazelle & Lembège, 2021). Later, between 21:22 and 22:05 UT (interval not shown), the upstream plasma contained clear periodic wave packets at the local proton cyclotron frequency (proton cyclotron waves or PCWs). These waves are a clear signature of the presence of unstable proton distributions due to the ionisation of exospheric neutral hydrogen in the SW, already at large distances from the planet (e.g., Mazelle et al., 2004; Romanelli et al., 2016; Romeo et al., 2021).

The magnetic field intensity and electron density fluctuations were first in phase in the SW and in the close vicinity of the shock (Figure 1a), changed to mostly an antiphase behavior deeper in the magnetosheath (representative of mirror mode-type waves) with the presence of very large amplitude *B*-field peaks, and then switched back to in-phase behavior in the MPB (indicative of fast magnetosonic waves or FMS, see Ruhunusiri et al., 2015). A clear magnetic pile up was observed with a *B*-field intensity steeply increasing from 10 nT to about 30 nT, coinciding with a substantial decrease in the ion and electron fluxes.

As described in Section 2.3, we use a two-step characterization of the wave environment to ascertain the nature of the waves in the magnetosheath. The first step, shown in Figure 2, performs a magnetic field cross-spectral analysis, with compressive $B_{||}$ and transverse $B_{\perp}$ wave powers (Figures 2b and 2c), polarisation percentage (Figure 2d), ellipticity (Figure 2e), and polarisation angle (Figure 2f, in the spacecraft rest frame). The local proton cyclotron frequency f_{ic} is superimposed as a solid line. Apart from true plasma waves making up the bulk of the wave power, the *B*-field dynamic spectra also captured faint high-frequency signals, mostly seen at a constant frequency, which we attribute to spacecraft effects on the instrument, such as reaction wheels

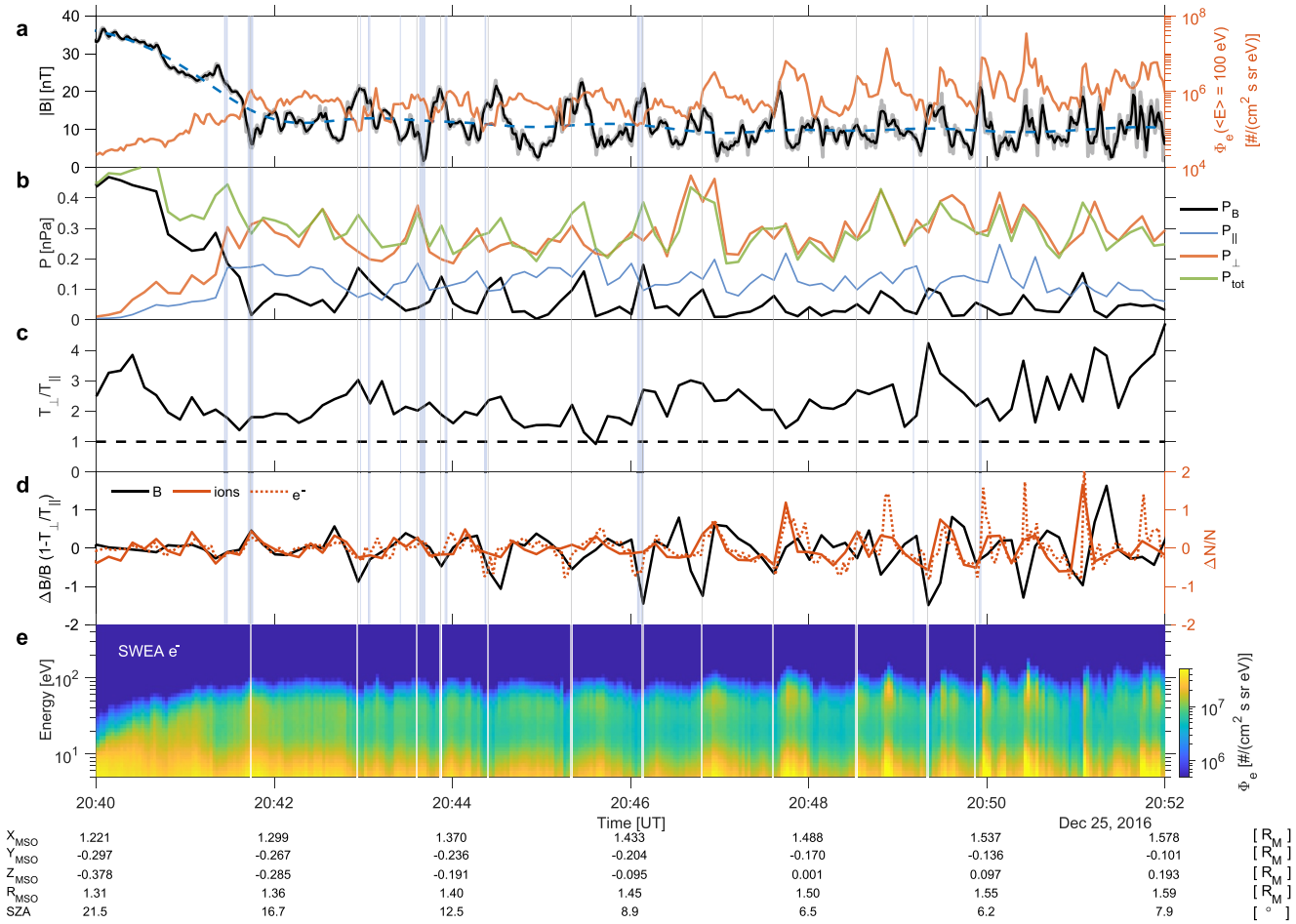

Figure 3. Event 1 Q-⊥ magnetosheath on 25 Dec. 2016 around 20:45 UT. (a) Total magnetic field at 1/32-s (gray line) and 2-s resolutions (black line) with low-pass filtered background field (dashed blue line, left axis), and 2-s resolution electron omnidirectional flux Φ_e at $\langle E \rangle = 100$ eV energy (right axis). (b) 8-s resolution magnetic pressure P_B, parallel and perpendicular ion thermal pressures $P_{||}$ and $P_{\perp}$, and total scalar pressure defined as $P_{\rm tot} = P_B + \frac{1}{3}\left(P_{||} + 2P_{\perp}\right)$. (c) Ion temperature anisotropy $T_{\perp}/T_{||}$ for ions. (d) Right and left terms of Equation 2, with relative density fluctuations $\Delta N/N$ for ions (red continuous line, left axis) and electrons (red dotted line, right axis). (e) Electron omnidirectional flux Φ_e. On panels (a–d) vertical blue areas correspond to automatic MiMo B-field only detections. Thin vertical gray lines mark where mirror modes are present, when considering ion data from Equation 2.

(Connerney, Espley, DiBraccio et al., 2015). Such signatures, clearly appearing in the polarisation panels, should be ignored. In the plasma upstream of the shock, linearly and LH circularly polarized noncompressive waves propagating along the MFA direction dominated, located around $f_{\rm ic}$. The LH wave modes in the spacecraft frame are consistent with the presence of pickup ions in the region upstream of the shock exciting the ion-ion electromagnetic instability (Mazelle et al., 2004; Romanelli et al., 2013, 2016), as also expected from α_{BV} values close to 90° (Table 1 and Figure 1d) and linear theory (Gary, 1991). Downstream of the shock in the magnetosheath, the wave modes changed to obliquely and fully transverse-propagating wave modes (polarisation angles >45°), mostly linearly polarized at or below $f_{\rm ic}$. This is consistent with the presence of compressive ULF waves of the fast mode type and mirror modes. At and around the MPB (20:35–20:40 UT), perpendicularly-propagating linearly polarized wave modes below 1 Hz (around $f_{\rm ic}$) coincided with the presence of *B*–*N* in-phase waves that were FMS in nature (lower frequencies) and the appearance of heavy ions in the STATIC signal.

In a second step, we look more precisely at the interval containing the MiMo candidates, as shown in Figure 3, with total magnetic field intensity and the 2-s electron flux at 100 eV energy (Figure 3a), the magnetic field, ion partial pressures and total scalar pressures (Figure 3), the ion temperature anisotropy (Figure 3c), the two terms of Equation 2 (Figure 3d) and the electron omnidirectional flux spectrum (Figure 3e, including secondary electrons dominating below 20–30 eV). We superimpose as blue vertical lines the compressive linearly polarized "MiMo-

like candidate" structures automatically detected following Simon Wedlund et al. (2023) (see Section 2.3) and compare to the analysis in Figure 3d. Because the magnetic field was not in the FOV of SWIA, some uncertainty is expected in the determination of $T_{\parallel}$.

Based on their general characteristics, we confirm that the detected structures (shown as vertical blue lines) are MiMos indeed. First, they appeared as highly compressive magnetic field peak structures with $\Delta B_{\parallel}/|B|$ of the order of 2. Second, they were in clear B–N and B–Φ_e antiphase with good agreement between the separate terms of Equation 2 (Figure 3d, supplemented by the SWEA density fluctuations). These field fluctuations were modulated by an ion temperature anisotropy of about 2 on average, steadily increasing with time upstream of the MPB, as expected from a Q-⊥ geometry. Third, these structures were also close to being in pressure balance, as shown in Figure 3b, in agreement with theoretical expectations (Gary, 1992).

Many other wave structures similar to the MiMo-like candidates were not captured by the **B** field-only algorithm of Simon Wedlund et al. (2023), a known caveat of the method and of the very stringent detection criteria used. These additional structures, fulfilling Equation 2 and thus having typical MiMo characteristics, are marked as vertical gray lines in Figure 3. From 20:43 UT to about 20:50 UT, most MiMo structures were B-field peaks, that is, structures that have positive $\Delta B_{\parallel}/B$ (Figures 3a and 3b). Closer to the foot of the MPB, a clear MiMo structure was detected as a B-field dip, which may suggest a different origin or a structure at a different evolutionary stage. This particular dip had an identical morphology and location with respect to the MPB as the large MiMo structure found by Simon Wedlund, Volwerk, Mazelle et al. (2022), during a (similar) Q-⊥ magnetosheath crossing on 2014-12-25, for Ls $\sim$260° and SZA$'$ $\sim$ 50°. All structures detected were clearly seen in the electron flux spectra, with an almost symmetric wave-like variation in flux and energy, where peaks in energy and flux coincided with the dips in-between the B-field peaks.

3.2. Event 2: Q-|| Magnetosheath, High Exospheric Season

Event 2, shown in Figure 4, is similar in context to the one discussed in Collinson et al. (2018). As for Event 1, PCWs extended far upstream of the nominal shock, well beyond 06:30 UT (not shown). The α_{BV} angle in the SW was 156° on average (Figure 4d), which favors the RH ion-ion electromagnetic instability over the LH mode according to linear theory (Gary, 1991). All of these aspects are indicative of a combination of two factors, an extended foreshock in a Q-|| geometry and an extended hydrogen exosphere (same Ls condition as Event 1), with backstreaming ions creating ULF foreshock waves, mixed with pickup ion-related waves. Downstream of the Q-|| shock (time before 05:59:30 UT) in the magnetosheath, B-field fluctuations were both larger and faster than those in Event 1, as expected from the Q-|| shock geometry and the turbulence that results from it. The MPB's magnetic pileup was not as steep as in Event 1 and started around 05:47 UT, with the spacecraft probing the magnetosphere 2 minutes earlier.

As shown in Figure 5, in the magnetosheath, the wave modes remained linearly polarized, strongly propagating perpendicularly to the MFA direction, which is consistent with the presence of compressive ULF waves of the fast mode type and mirror modes, especially in the deep magnetosheath where the $B_{\parallel}$ power dominated. At and around the MPB, the cross-spectral frequency analysis reveals a behavior consistent with B–N in-phase compressive waves that are FMS in nature (lower frequencies) and with the appearance of heavy ions in the STATIC signal (higher frequencies).

In Figure 6, MiMo-like structures (first marked as blue vertical lines) displayed a much more turbulent behavior than in Event 1, with a moving skewness analysis revealing a change from peaks to dips and intervals of mixed behavior (quasi-sinusoidal) the closer the spacecraft was to the MPB, with $\Delta B/|B|$ of the order of 0.5–1. This is most likely the result of the intrinsically higher turbulence of the Q-|| magnetosheath as opposed to that of Q-⊥ of Event 1. The same wavy behavior in the electron flux spectra (Figures 6a and 6e) found for Event 1 also took place for Event 2, with instrumental secondary electrons present below 25 eV. Antiphase between plasma density or electron flux and magnetic field variations modulated by the temperature anisotropy was fulfilled well throughout the interval, especially between about 05:48 and 05:55 UT (Figure 6d). Moreover, in contrast to Event 1, the ion temperature anisotropy remained most of the time below 2. It fluctuated much less in the time interval considered, with the quasi-sinusoidal B-field variations corresponding to a minimum anisotropy of about 1.5. Finally, as for Event 1, a clear B-field dip was observed at the foot of the MPB around 05:47:20 UT, exhibiting textbook MiMo behavior (Simon Wedlund, Volwerk, Mazelle, et al., 2022). Following the same arguments as for Event 1 (B-N_e

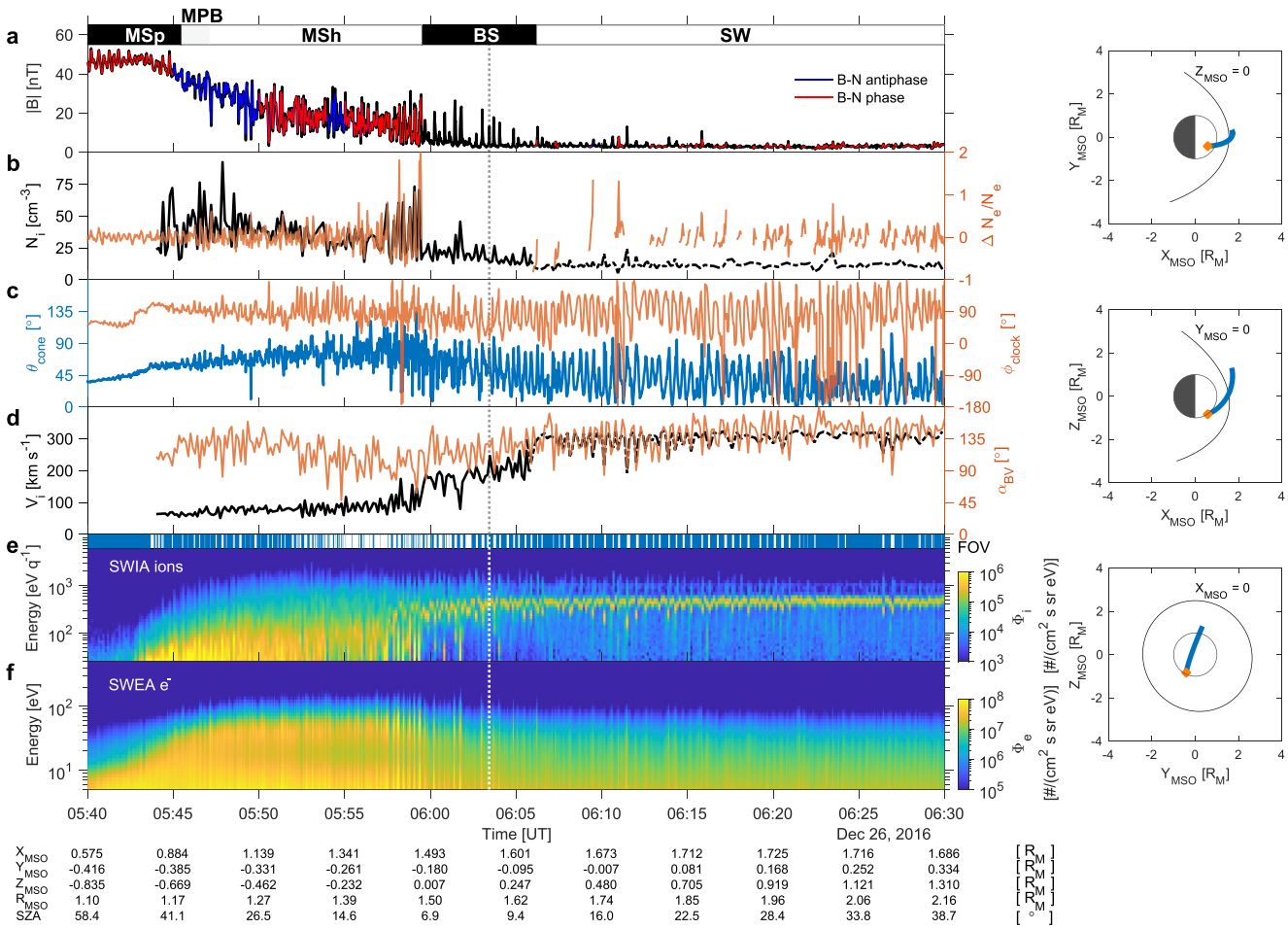

Figure 4. Overview of Event 2 and the Martian Q-|| shock crossing on 26 Dec. 2016 around 06 UT, Ls = 247°. Same format as Figure 1.

antiphase and Equation 2 fulfilled, approximate pressure balance, see Gary, 1992), we conclude that all the structures marked as gray vertical lines on Figure 6 are true MiMos.

4. Mirror Mode Generation

Since the Q-⊥ shock is usually the main source of temperature anisotropy necessary for MiMos to grow in the magnetosheath (e.g., Gary, 1992; Tsurutani, Lakhina, et al., 2011), the surprising presence of magnetosheath MiMos downstream of a Q-|| shock raises the question of how they were generated in this case. In this section, we first examine whether the MiMos in Events 1 and 2 were generated locally or remotely with respect to their place of detection in the magnetosheath, and, second, we identify the source of the free energy at the origin of the waves.

4.1. Local or Remote Wave Generation?

In Event 1, we observed a predominance of magnetic peaks in the middle of the magnetosheath. In Event 2, magnetic peaks were first seen, with intervals of quasi-sinudoidal variations, growing more toward dips the closer MAVEN was to the MPB. This evolution is a marker of the nonlinear temporal evolution of MiMos (e.g., Génot et al., 2001; Génot et al., 2009; Joy et al., 2006; Kuznetsov et al., 2008; Passot et al., 2006; Passot & Sulem, 2008; Soucek et al., 2008). From theoretical and numerical kinetic simulation considerations, the nonlinear saturation of the mirror instability has indeed been shown to first lead to the formation of magnetic peaks instead of dips (Califano et al., 2008; Tsurutani, Echer, et al., 2011). This suggests that the MiMo structures detected in Events 1 and 2 are relatively young structures, close to their region of generation. To obtain some insight into the temporal

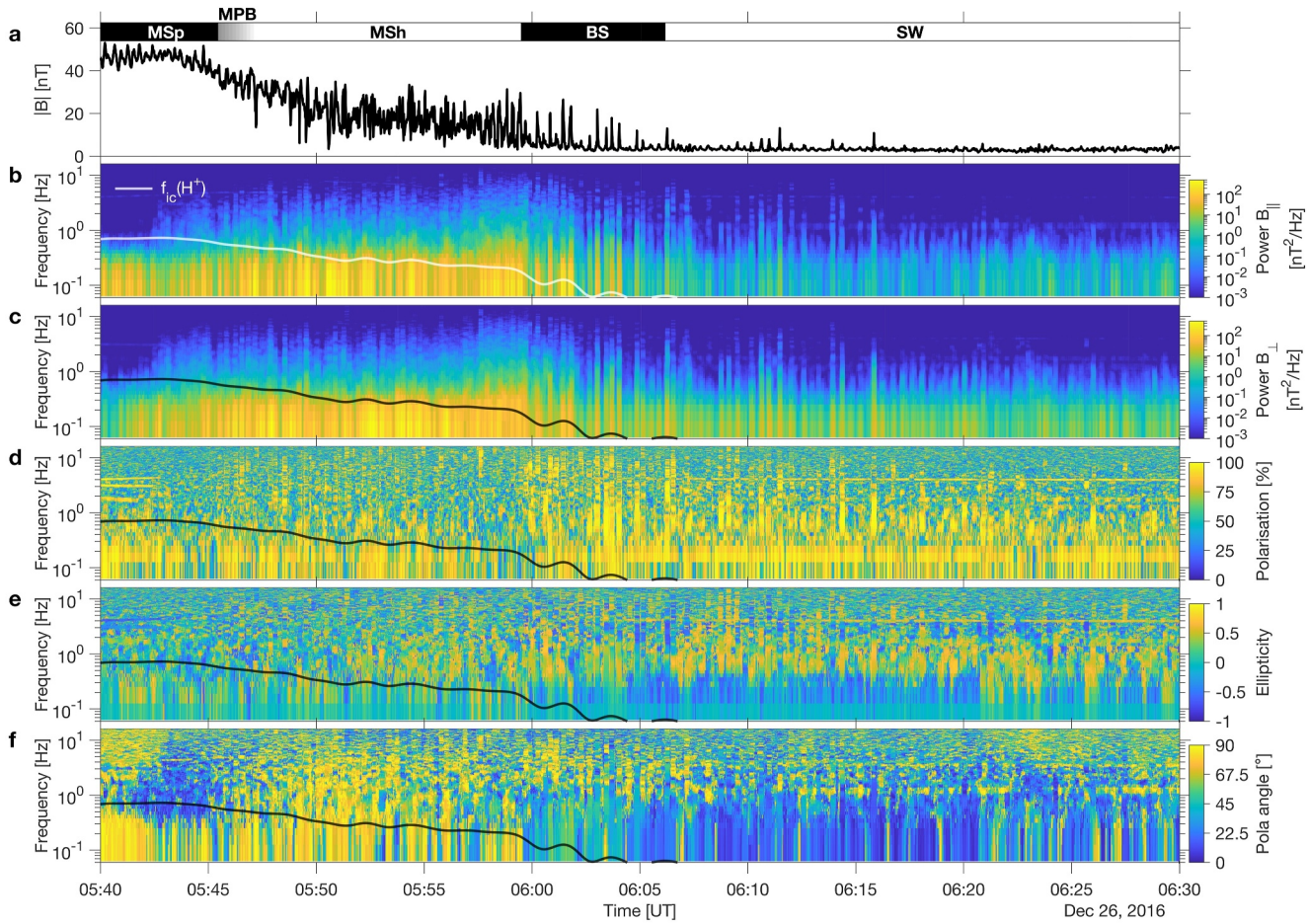

Figure 5. Cross spectral analysis of **B** in the spacecraft rest frame for Event 2 (Q-||, Ls = 287°) in the spacecraft frame. Same format as Figure 2.

evolution of the structures, we now study how the MMIC evolves throughout the magnetosheath for Events 1 and 2, and calculate the maximum linear growth rate of the mirror instability near threshold.

4.1.1. Evolution of Mirror Mode Instability Through the Magnetosheath

Figure 7a displays the MMIC (see Equation 1) of Events 1–3. We first determine the normalized radial distance F of the spacecraft in the magnetosheath introduced in Earth studies (Dimmock et al., 2020; Génot et al., 2009; Verigin et al., 2006). F is a fraction defined as:

$$F = \frac{R_{\mathrm{MSO}} - r_{\mathrm{MPB}}}{r_{\mathrm{shock}} - r_{\mathrm{MPB}}}, \tag{3}$$

where R_{MSO} is the spacecraft radial distance from the planet, r_{shock} is the radial distance of the shock along the spacecraft orbit, and r_{MPB} is the radial distance of the MPB location. Thus, $F = 0$ at the MPB and $F = 1$ at the shock. Because of the chosen subsolar geometry and the mostly radial plasma velocity (along the $-X_{\mathrm{MSO}}$ direction) in the magnetosheath, F is a good absolute measure of the size of the magnetosheath, even if SW upstream conditions vary.

Events 1 and 2 display two very different behaviors. Close to the MPB ($F = 0$), the plasma was in marginal stability for both events until about $F = 0.1$. At this point, the MMIC for Event 1 (blue line) became strongly negative (the plasma was unstable to the generation of mirror modes) and seemed to increase with increasing F to reach very large negative values for $F > 0.6$. This is consistent with the temperature anisotropy necessary for the

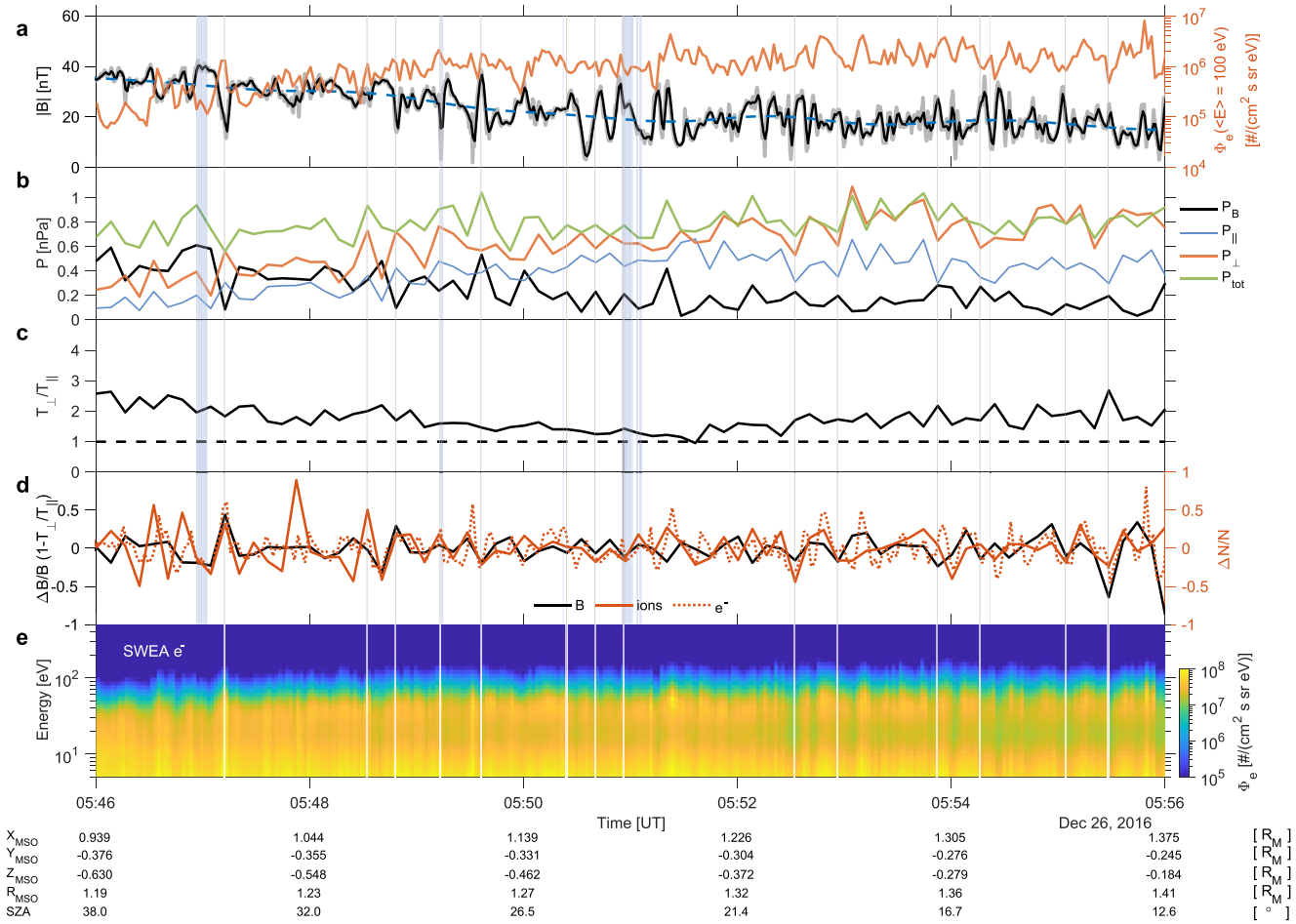

Figure 6. Event 2 Q-|| magnetosheath on 26 Dec. 2016 around 05:50 UT. Same format as Figure 3.

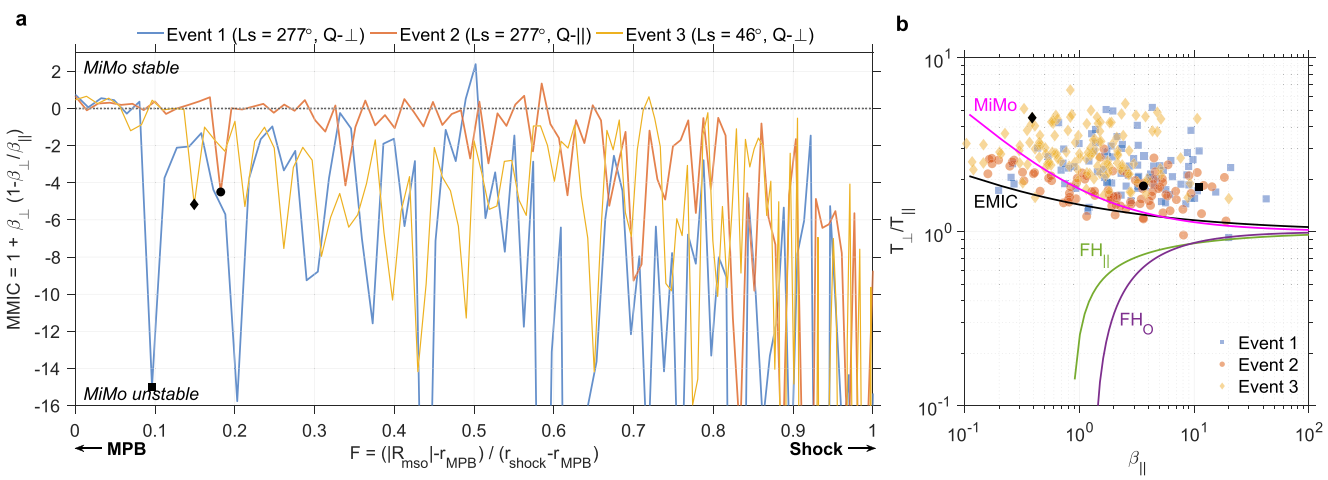

Figure 7. (a) Mirror mode instability criterion as a function of normalized fraction F of the magnetosheath with MiMo-unstable conditions for MMIC<0. (b) "Brazil plot" of temperature anisotropy with respect to ion plasma $\beta_{||}$ for the three events studied. On (b), we superimpose the instability thresholds for electromagnetic ion cyclotron (EMIC), mirror modes (MiMo), parallel firehose ($FH_{||}$ and oblique firehose (FH_O) calculated by Hellinger et al. (2006) in the linear regime. The filled black square, circle and diamond are the identified magnetic field dips close to the magnetic pileup boundary for Events 1, 2 and 3, respectively.

instability to grow being created just downstream of the Q-⊥ shock, in the $F = 0.7$–1.0 region, as also seen in Figures 3c and 6c. In contrast, the MMIC for Event 2 (red line) remained at marginal stability up to $F = 0.6$ and only grew toward larger negative values for $F \gtrsim 0.85$, where the turbulence due to the shock started to play a role. As a comparison, we also calculate the MMIC of Event 3 (yellow line, Q-⊥ magnetosheath, low exospheric activity, see Table 1). The MMIC of Event 3 appears to lie in-between the other two events', especially for $F \in [0, 0.25]$ and $F \in [0.6, 0.95]$, suggesting an intermediate case between Events 1 and 2 with respect to the instability.

Theoretically, no significant temperature anisotropy due to the shock is expected downstream of a Q-|| shock (Event 2). If some temperature anisotropy is present around the shock, it is mostly inherited from the SW turbulence upstream and that created around the shock. This suggests that the source of the anisotropy creating the MiMo structures may be (a) transported downstream from the source of the turbulence, and/or (b) located closer to the detection area of the structures. In hypothesis (a), the shock-inherited turbulence is not expected to be quenched rapidly because the large amplitude of the plasma and magnetic field fluctuations do not have the space and time to do so in the relatively small magnetosheath considered here. Because of how stable the profile of the MMIC of Event 2 is from the middle of the magnetosheath downstream to the MPB, we thus favor hypothesis (b) and a local generation by another pressure anisotropy-driven mechanism. The nature of this extra source of anisotropy is discussed in Section 4.2.

Figure 7b displays for each event the "Brazil" plot of plasma instabilities, which collects the data in the $T_\perp/T_\parallel$–$\beta_\parallel$ plane (e.g., Verscharen et al., 2019). We superimpose the four main proton plasma instability thresholds calculated for a bi-Maxwellian plasma at a growth rate of $10^{-3}\Omega_{ci}$, where $\Omega_{ci} = 2\pi f_{\rm ci}$ is the proton cyclotron angular frequency (Hellinger et al., 2006). The plasma of Event 2 clusters around the marginal stability line of the MiMo instability. The two Q-⊥ events, Events 1 and 3, display a much more spread-out distribution of values with most of them lying largely above the MiMo threshold. This contrasting behavior implies a difference of origin and evolution for these magnetosheaths. More precisely, simulations, such as the noise-free kinetic Vlasov-Maxwell 1D simulations of Califano et al. (2008), have shown that, for $\beta \sim 1$, magnetic peaks that are formed relatively far from the MMIC threshold can evolve, in time, into magnetic dips, confirming the Cluster observations of Soucek et al. (2008) at Earth. This suggests that the signatures in Events 1 and 3, partially or wholly generated from a remote source of free energy close to the bow shock, have had more time to evolve than the signatures in Event 2.

Finally, we highlight the prominent large B-field dips immediately before the MPB's magnetic ramp seen in all three events in Figure 7 (filled symbols). According to Califano et al. (2008) and Soucek et al. (2008), these magnetic dip structures should be generated some distance upstream of their detection location, in regions of relatively small $\beta_\parallel$–large $T_\perp/T_\parallel$. Events 2 and 3 appear to follow this prediction, but not Event 1. The reason for this difference is not known but may be in part due to SWIA's different FOV.

4.1.2. Growth Rate

To evaluate the time needed for the observed MiMos to grow, we now calculate the maximum growth rate of the linear mirror instability near threshold, noted γ_m, as given for a bi-Maxwellian plasma with cold electrons by Hellinger (2007) (their Equation 17):

$$\gamma_m = \frac{\Omega_{ci}}{4\sqrt{3\pi}} \frac{\mathrm{MMIC}^2}{\beta_\perp \sqrt{\left(\frac{T_\perp}{T_\parallel}\right)^3 \left(1 + \frac{\beta_\perp - \beta_\parallel}{2}\right)}} \tag{4}$$

Although it may not be applicable for the wide range of values in the $\beta_\parallel$–$T_\perp/T_\parallel$ plane and the non-Maxwellian multi-species plasma found at Mars, Equation 4 can give a useful indication of the size of a MiMo structure with respect to that of the magnetosheath, by dividing the background bulk plasma speed in the $-X_{\rm MSO}$ direction with γ_m. Using linear solvers to calculate a more accurate growth rate of the MiMo structures in different conditions is left to a future study.

The MiMo growth characteristics are summarized in Table 2. In the typical MiMo dip structures closest to the MPB (see the three highlighted structures in Figure 7), γ_m was of the order of 0.15 s^{-1} for Events 1 and 2, that is, a minimum distance for wave growth of about $d_m = 500$ km. This is significantly less than the size of the subsolar magnetosheath, especially for Event 2 where the magnetosheath had an estimated radial width of 1,700 km. This

Table 2
Typical Characteristics of Mirror Modes Found Closest to the Magnetic Pileup Boundary for Events 1, 2 and 3, With Maximum Growth Rate of the Instability Calculated Using Equation 4

Parameters	Units	Event 1 20:41:44 UT	Event 2 05:47:12 UT	Event 3 08:47:58 UT	Remark
Ω_{ci}	s^{-1}	0.73	2.15	1.10	Ion cyclotron frequency
$\beta_\perp$	–	12.0	6.6	1.8	Perpendicular ion plasma β
$\beta_\parallel$	–	5.0	3.6	0.4	Parallel ion plasma β
$T_\perp/T_\parallel$	–	2.4	1.8	4.5	Ion temperature/pressure anisotropy
MMIC	–	−15.8	−4.5	−5.2	Mirror mode instability criterion (Equation 1)
γ_m	s^{-1}	0.16	0.14	0.18	Maximum growth rate (Equation 4)
γ_m/Ω_{ci}	–	0.21	0.07	0.16	Maximum normalized growth rate
$\langle\lvert\mathbf{U}_p\rvert\rangle$	km s^{-1}	76	79	152	Average bulk plasma speed
d_m	km	495	580	865	Distance for linear wave growth
d_{MSh}	km	1,050	1,700	1,450	Radial size of the magnetosheath
ΔF_m	–	0.47	0.34	0.60	Normalized sheath distance for wave growth

Note. The minimum distance d_m needed for the growth of the mirror mode is calculated as $\langle\lvert\mathbf{U}_p\rvert\rangle/\gamma_m$, where $\langle\lvert\mathbf{U}_p\rvert\rangle$ is the average plasma bulk speed in this region, assumed radial. The size of the magnetosheath assumes a radial geometry from the observed MPB crossing to that of the observed shock. The values below are given for the structures with maximum growth rate closest to the MPB, found in the dips of *B*-field fluctuations.

result implies that MiMo structures were created within about $\Delta F_m = 0.3$ of their detection region. For Event 3, d_m was closer to 900 km, that is, more comparable to the full width of the magnetosheath.

Consequently, reinforcing the conclusions of Section 4.1.1, we argue for a more local generation of MiMos in Events 1 and 2 as compared to Event 3, for which the (remote) Q-⊥ shock is expected to play the major role in the creation of free energy for the waves.

4.2. Nature of MiMo Generation: Unstable Pickup Protons

As shown in Section 4.1, the source of the anisotropy at the origin of the MiMos in Events 1 and 2 is close to the detection region of the waves. We now focus on determining the origin of the local temperature anisotropy at the origin of the MiMos.

A good candidate for a local source of anisotropy is the pickup ion contribution. As described in Section 3, the presence of PCWs upstream of the shock is the unmistakable signature of unstable pickup protons VDFs in the SW, born from an extended hydrogen exosphere. Such an exosphere is expected to have an increased density the closer to the planet, and thus an increased production of unstable pickup distributions. Together with Collinson et al. (2018) who described events close to the same dates as ours, this is fully consistent with the observed large extension and high-density of the hydrogen exosphere for such a Ls condition (Clarke et al., 2017; Halekas, 2017; Rahmati et al., 2017; Romanelli et al., 2016).

In order to investigate this hypothesis in more detail, we concentrate on Event 1, where MiMos are well defined and have sufficiently long duration for the SWIA data sets to be most meaningful, and show the ion and electron pitch-angle distributions in the plasma rest frame (Figures 8b and 8c). As explained earlier, Event 1 is expected to have both sources of temperature anisotropy at play, local and remote, with an average angle α_{BV} between the local magnetic field direction and the plasma velocity direction of 90° at the time when MiMo were detected, suggesting the production of a ring-type ion velocity distribution in the plasma rest frame, as expected and observed at comets (see Brinca, 1991; Huddleston & Johnstone, 1992). We highlight in the total magnetic field intensity of Figure 8a, downsampled to SWEA's resolution of 2 s, the most prominent *B*-field dips corresponding to MiMos.

From theoretical considerations, the newborn ion distribution is expected to be a cold beam with velocity equal to $-\mathbf{V}_p$ in the plasma rest frame, with $\mathbf{V}_p$ the bulk plasma velocity in the source region. Moreover, pickup ion fluxes

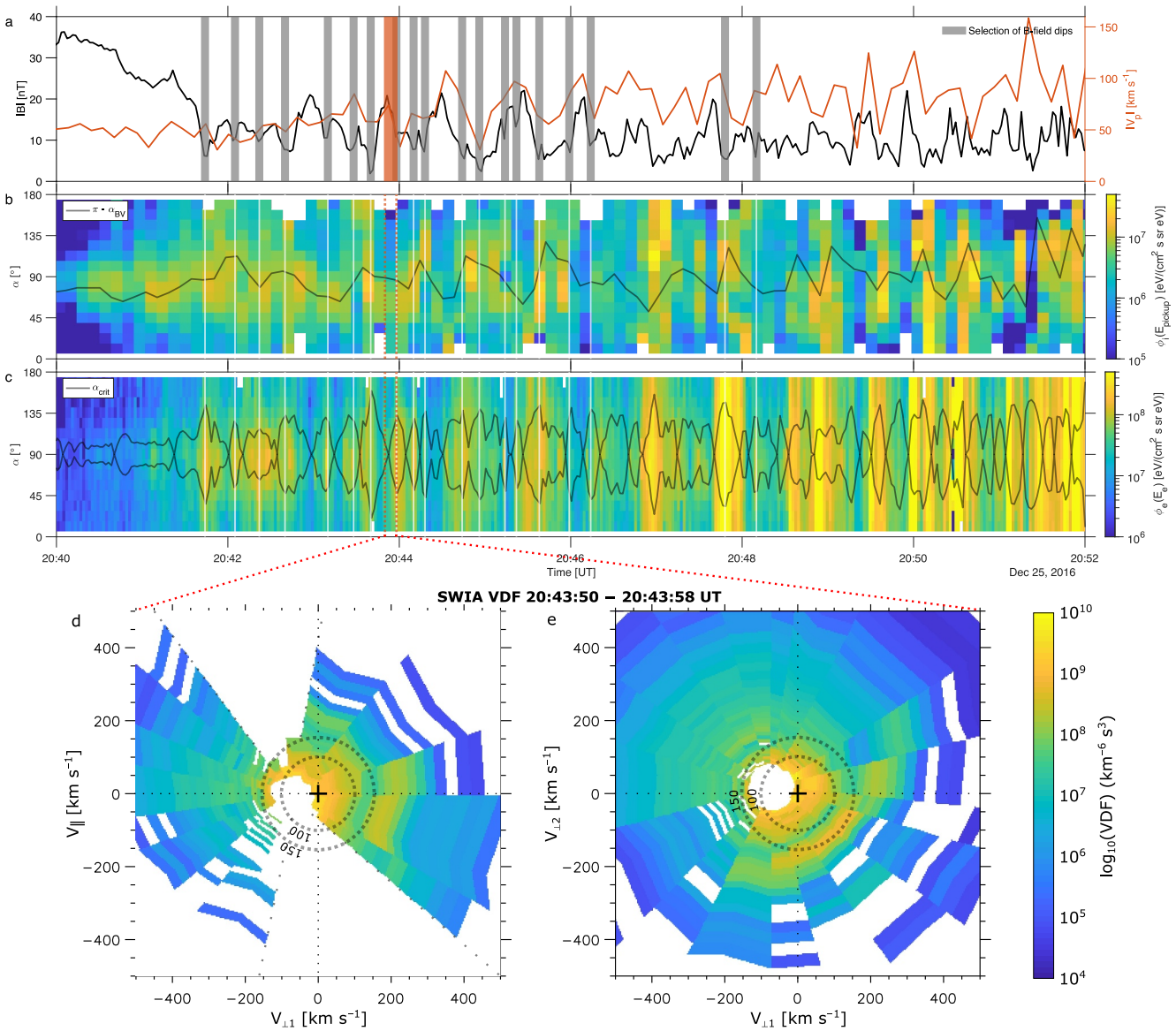

Figure 8. Ion and electron pitch-angle distributions (PADs) for Event 1 in the magnetosheath plasma rest frame. (a) Total magnetic field. (b) SWIA ion energy differential fluxes versus time and PAD at the local newly injected pickup proton energy in the $E_{\text{pickup}} = 40$–100 eV range in the plasma rest frame. (c) SWEA electron energy differential fluxes versus time and PAD for an energy of $E_e = 100$ eV. (d, e) SWIA ion velocity distribution functions measured in the plasma rest frame between 20:43:50 UT and 20:43:58 UT, in the $V_{\perp 1}$–$V_\parallel$ and $V_{\perp 1}$–$V_{\perp 2}$ planes, with superimposed contours of equal velocities at 100 and 150 km s^{-1}. In panel (a), a selection of the most prominent B-field dips is highlighted in gray.

are expected to concentrate at angles close to π–α_{BV}, which is the initial pitch angle at the injection point in velocity space (Delva et al., 2011, and references therein). In Figure 8b, the ion pitch-angle distributions (PADs) are shown at the average energy of the pickup ions in this region so that $\langle E_{\text{pickup}} \rangle \approx 40$–$100$ eV, assuming protons dominate the plasma. In the chosen interval, the maxima of energy fluxes are strikingly located around π–α_{BV}, especially in the first interval of time containing MiMo dips and peaks. This is a first strong indication that pickup ions, and in particular here pickup protons, are present in the plasma and may be a source of the local plasma instability at the origin of MiMos.

A second indication of the role of pickup protons in the local generation of MiMos can be seen in Figures 8d and 8e, where we plot an example of VDF in the $V_\parallel$–$V_{\perp 1}$ and $V_{\perp 1}$–$V_{\perp 2}$ planes of velocity phase space captured by SWIA in one of the bigger MiMo peak structures close to the MPB. The parallel component is defined, as before,

as the 8-s averaged normalized **B**-field direction $\left(\mathbf{e}_{\parallel} = \mathbf{B}/|\mathbf{B}|\right)$, whereas the first perpendicular direction is obtained by finding the perpendicular direction to **B** in the $(\mathbf{B}, \mathbf{V}_i)$ plane (noted $\mathbf{e}_{\perp 1}$) and the second perpendicular direction by calculating $\mathbf{e}_{\perp 2} = \mathbf{e}_{\parallel} \times \mathbf{e}_{\perp 1}$. The VDFs presented here were chosen among many available in the SWIA data sets as a compromise between FOV and a relatively good separation between ion populations in energy and angle. In Figure 8d, the empty angular sectors correspond to angular detection limitations due SWIA's FOV. Despite this limitation, a local thermal magnetosheath population can be identified at the center of the distribution at $\left(V_{\parallel}, V_{\perp 1} = 0\right.$ (position of the black cross). A second ion population was also present at significantly higher velocities, at the edge of two angular sectors close to $V_{\parallel} = 0$, with $V_{\perp 1} \in [150, 200]$ km s^{-1}. The limited scattering in angle in this population is compatible with the idea that the pickup protons were at the beginning of their gyration motion around **B** and did not had the time to scatter much in angle.

Because α_{BV} is close to 90°, the expected newly picked-up proton distribution is a pure ring distribution in the plasma rest frame (Szegö et al., 2000). This is what is seen in Figure 8e, where the VDF exhibited two main populations: the thermal plasma around the center of the velocity space, and a suprathermal population that appears on a partial angular ring located at an isocontour of velocity between 100 and 150 km s^{-1} for $V_{\perp 2} < 0$. Given that the loci of productions of newborn ions must be upstream of the observation point for the instability to grow (e.g., Brinca, 1991), the value of the bulk plasma velocity at the injection time should be larger than the local one. Moreover, the typical linear growth rates of the MiMo structures in Event 1 (see Table 2) imply that the injection points were located close to the middle of the magnetosheath, where bulk plasma velocities were of the order of 100 km s^{-1}, in broad agreement with the typical ring energy values.

Besides pickup protons, a possible excitation source for the MiMos in Event 1 may be from gyrating ions with large Larmor radii that have been specularly reflected at the Q-⊥ shock and which explore an extended region downstream. Indeed, such ions form ring-type distributions in the plasma frame (Gosling & Robson, 1985) and may contribute to the local increase of the temperature anisotropy, with their characteristic energies exceeding that of the background thermal plasma. Such populations have previously been reported at Mars in the magnetosheath and even downstream of the MPB because of finite Larmor radius effects (Harada et al., 2019). Given the shock geometry of the shock (Q-⊥) and following Decker (1988) and Meziane et al. (2004), we found a bulk velocity of specularly reflected ions in the plasma rest frame of the order of 600 km s^{-1}, which seems inconsistent with the VDF observations of Figures 8d and 8e. Consequently, although this anisotropy source cannot be completely ruled out, the contribution of gyrating ions to the local generation of MiMos does not seem to play the major role here. In the case of Event 2 (Q-|| shock), no specularly gyrating ion are expected as they are reflected upstream in the foreshock as backstreaming ions and do not contribute to the local anisotropy in the magnetosheath (Meziane et al., 2004).

Additionally, as a complement to the ion observations, we show in Figure 8c the electron flux spectra and superimpose onto the high-energy electron PADs the critical pitch angle α_{crit} at which particles become trapped in MiMo dip structures (Kivelson & Southwood, 1996; Soucek & Escoubet, 2011):

$$\arcsin\sqrt{\frac{B}{B_{\max}}} < |\alpha_{\text{crit}}| < \frac{\pi}{2}. \tag{5}$$

This critical angle nicely delimits the regions of maximum electron fluxes (shown here at 100 eV), with suprathermal electrons with pitch angles close to 90° dominating the plasma, and a depletion of electron fluxes at low pitch angles. MiMos thus appeared efficient in trapping these high-energy electrons between 08:41 and 08:47:30 UT, at which point the electron PADs became much more isotropic, a trend increasing the closer the spacecraft ventured to the shock. This change in behavior coincided with the progressive disappearance of MiMo structures, with B and N gradually becoming in phase, a behavior more reminiscent of fast-mode-type hydrodynamic waves produced downstream of the shock. Fluctuations in this region might have in part grown from the free energy available immediately downstream of the Q-⊥ shock.

5. Conclusions

At Earth, the major source of the temperature anisotropy at the origin of mirror modes (MiMo) is the Q-⊥ shock (Gary, 1992). This source is also present at Mars (Simon Wedlund, Volwerk, Mazelle, et al., 2022). For the first

time, we show in the present paper the unmistakable existence at Mars of another source of temperature anisotropy at the origin of MiMos, namely, unstable pickup proton distributions due to the presence of an extended exosphere of neutral hydrogen around the planet. This source acts everywhere around Mars, may affect the shock structure (see Lu et al., 2013, as shown at Venus), and is expected to evolve with the exospheric seasons, with a sizable effect at the maximum of exospheric activity around solar longitude Ls $\sim$ 270°.

The pickup ion instability source is reminiscent of temperature anisotropy-generating mechanisms found at comets (Mazelle et al., 1991; Price, 1989), which have an expanding atmosphere that also varies in time, and around the outgassing moons of Jupiter deep in the giant magnetosphere of Jupiter (Huddleston et al., 1999, 2000; Russell et al., 1999). More precisely, we show that the Martian environment uniquely holds a multiplicity of favorable conditions for temperature-driven instabilities such as mirror modes, including newborn ions that are subsequently picked up by the local electric field (Events 1 and 2), in addition to the classical Q-⊥ shock source (Events 1 and 3). These favorable conditions may explain why, despite its small size with respect to the planet, a weak induced magnetosphere and a heavy plasma turbulence, the Martian magnetosheath may be on average mostly stable with respect to most instabilities by the time the plasma reaches the inner boundaries of the system (see Espley et al., 2004; Jin et al., 2022; Wang et al., 2020).

The next step is to quantify each temperature anisotropy-generating mechanism with respect to seasons, upstream conditions and SW transient occurrences, and compare those with the intrinsic plasma turbulence in the magnetosheath. Studying this aspect would lead to a better understanding of how plasma instabilities process and transform the endless supply of energy and momentum from the SW, and transmit it into the inner magnetosphere of Mars, with, as of yet understudied, consequences on the evolution of the atmosphere (Collinson et al., 2018; Fowler et al., 2018). Such a question should be investigated not only with MAVEN but also with the help of global hybrid kinetic simulations of the environment of Mars, Venus, Mercury and comets (see for example Behar et al., 2022; Jarvinen et al., 2020a; Jarvinen et al., 2020b, 2022).

Data Availability Statement

The calibrated MAVEN data sets, including MAG, SWIA, SWEA and STATIC are available from the NASA Planetary Data System (PDS) at https://pds-ppi.igpp.ucla.edu/mission/MAVEN. Predicted bow shock times, spatial coordinates and shock geometry (θ_{Bn}) for the 2014–2021 data set (up to Mars Year 35) are available on Zenodo at https://doi.org/10.5281/zenodo.5725288 (Version 3, Simon Wedlund et al., 2021).

Acknowledgments
This research is funded by the Austrian Science Fund (FWF) 10.55776/P35954. Parts of this work for the observations obtained with the SWEA instrument are supported by the French space agency CNES (National Centre for Space Studies). The authors acknowledge the use of the CLWeb viewing and analysis software (v.16.57) developed at IRAP (France) by E. Penou. CSW thanks V. Génot (IRAP, Toulouse), Z. Vörös and A. Settino (IWF/ÖAW, Austria) for helpful discussions, and M. Simon Wedlund for numerous creative discussions, unwavering support and early feedbacks on this idea.

References

Andreone, G., Halekas, J. S., Mitchell, D. L., Mazelle, C., & Gruesbeck, J. (2022). Properties of electron distributions in the Martian space environment. *Journal of Geophysical Research: Space Physics*, *127*(1), e2021JA029404. https://doi.org/10.1029/2021JA029404

Balikhin, M. A., Sagdeev, R. Z., Walker, S. N., Pokhotelov, O. A., Sibeck, D. G., Beloff, N., & Dudnikova, G. (2009). THEMIS observations of mirror structures: Magnetic holes and instability threshold. *Geophysical Research Letters*, *36*(3). https://doi.org/10.1029/2008GL036923

Behar, E., Fatemi, S., Henri, P., & Holmström, M. (2022). *Menura*: A code for simulating the interaction between a turbulent solar wind and solar system bodies. *Annals of Geophysics*, *40*(3), 281–297. https://doi.org/10.5194/angeo-40-281-2022

Bertucci, C., Mazelle, C., Crider, D. H., Mitchell, D. L., Sauer, K., Acuña, M. H., et al. (2004). MGS MAG/ER observations at the magnetic pileup boundary of mars: Draping enhancement and low frequency waves. *Advances in Space Research*, *33*(11), 1938–1944. https://doi.org/10.1016/j.asr.2003.04.054

Brinca, A. L. (1991). Cometary linear instabilities - from profusion to perspective. *Geophysical Monograph Series*, *61*, 211–221. https://doi.org/10.1029/GM061p0211

Brinca, A. L., & Romeiras, F. J. (1998). On the stability of stationary nongyrotropic distribution functions: Coupling and purely growing waves. *Journal of Geophysical Research*, *103*(A5), 9275–9284. https://doi.org/10.1029/97JA01995

Burgess, D., Lucek, E. A., Scholer, M., Bale, S. D., Balikhin, M. A., Balogh, A., et al. (2005). Quasi-parallel shock structure and processes. In G. Paschmann, S. J. Schwartz, C. P. Escoubet, & S. Haaland (Eds.), *Outer magnetospheric boundaries: Cluster results* (Vol. 20, pp. 205–222). Springer Netherlands. https://doi.org/10.1007/1-4020-4582-4_7

Burgess, D., & Scholer, M. (2015). *Collisionless shocks in space plasmas: Structure and accelerated particles*. Cambridge University Press. https://doi.org/10.1017/CBO9781139044097

Califano, F., Hellinger, P., Kuznetsov, E., Passot, T., Sulem, P. L., & Trávníček, P. M. (2008). Nonlinear mirror mode dynamics: Simulations and modeling. *Journal of Geophysical Research*, *113*(A8). https://doi.org/10.1029/2007JA012898

Chandrasekhar, S., Kaufman, A. N., & Watson, K. M. (1958). The stability of the pinch. *Proceedings of the Royal Society of London A* (Vol. 245(1243), 435–455). https://doi.org/10.1098/rspa.1958.0094

Clarke, J. T., Mayyasi, M., Bhattacharyya, D., Schneider, N. M., McClintock, W. E., Deighan, J. I., et al. (2017). Variability of D and H in the Martian upper atmosphere observed with the MAVEN IUVS echelle channel. *Journal of Geophysical Research (Space Physics)*, *122*(2), 2336–2344. https://doi.org/10.1002/2016JA023479

Collinson, G., Wilson, L. B., Omidi, N., Sibeck, D., Espley, J., Fowler, C. M., et al. (2018). Solar wind induced waves in the skies of mars: Ionospheric compression, energization, and escape resulting from the impact of ultralow frequency magnetosonic waves generated upstream of the Martian bow shock. *Journal of Geophysical Research (Space Physics)*, *123*(9), 7241–7256. https://doi.org/10.1029/2018JA025414

Connerney, J. E. P., Espley, J., Lawton, P., Murphy, S., Odom, J., Oliversen, R., & Sheppard, D. (2015a). The MAVEN magnetic field investigation. *Space Science Reviews*, *195*(1–4), 257–291. https://doi.org/10.1007/s11214-015-0169-4

Connerney, J. E. P., Espley, J. R., DiBraccio, G. A., Gruesbeck, J. R., Oliversen, R. J., Mitchell, D. L., et al. (2015b). First results of the maven magnetic field investigation. *Geophysical Research Letters*, *42*(21), 8819–8827. https://doi.org/10.1002/2015GL065366

Decker, R. B. (1988). Computer modeling of test particle acceleration at oblique shocks. *Space Science Reviews*, *48*(3–4), 195–262. https://doi.org/10.1007/BF00226009

Delva, M., Mazelle, C., & Bertucci, C. (2011). Upstream ion cyclotron waves at Venus and Mars. *Space Science Reviews*, *162*(1–4), 5–24. https://doi.org/10.1007/s11214-011-9828-2

Dimmock, A. P., Hietala, H., & Zou, Y. (2020). Compiling magnetosheath statistical data sets under specific solar wind conditions: Lessons learnt from the dayside kinetic southward IMF gem challenge. *Earth and Space Science*, *7*(6), e2020EA001095. https://doi.org/10.1029/2020EA001095

Espley, J. R., Cloutier, P. A., Brain, D. A., Crider, D. H., & Acuña, M. H. (2004). Observations of low-frequency magnetic oscillations in the Martian magnetosheath, magnetic pileup region, and tail. *Journal of Geophysical Research*, *109*(A7). https://doi.org/10.1029/2003JA010193

Ferrière, K. M., & André, N. (2002). A mixed magnetohydrodynamic-kinetic theory of low-frequency waves and instabilities in homogeneous, gyrotropic plasmas. *Journal of Geophysical Research*, *107*(A11), SMP7-1–SMP7-17. https://doi.org/10.1029/2002JA009273

Fowler, C. M., Andersson, L., Ergun, R. E., Harada, Y., Hara, T., Collinson, G., et al. (2018). MAVEN observations of solar wind-driven magnetosonic waves heating the Martian dayside ionosphere. *Journal of Geophysical Research: Space Physics*, *123*(5), 4129–4149. https://doi.org/10.1029/2018JA025208

Gary, S. P. (1991). Electromagnetic ion/ion instabilities and their consequences in space plasmas - A review. *Space Science Reviews*, *56*(3–4), 373–415. https://doi.org/10.1007/BF00196632

Gary, S. P. (1992). The mirror and ion cyclotron anisotropy instabilities. *Journal of Geophysical Research*, *97*(A6), 8519–8529. https://doi.org/10.1029/92JA00299

Gary, S. P., Fuselier, S. A., & Anderson, B. J. (1993). Ion anisotropy instabilities in the magnetosheath. *Journal of Geophysical Research*, *98*(A2), 1481–1488. https://doi.org/10.1029/92JA01844

Génot, V. (2008). Mirror and firehose instabilities in the heliosheath. *APJ*, *687*(2), L119–L122. https://doi.org/10.1086/593325

Génot, V., Budnik, E., Jacquey, C., Dandouras, I., & Lucek, E. (2009). Mirror modes observed with cluster in the Earth's magnetosheath: Statistical study and IMF/solar wind dependence. In *Advances in geosciences* (Vol. 14, pp. 263–283). World Scientific Publishing Company. https://doi.org/10.1142/9789812836205_0019

Génot, V., Schwartz, S. J., Mazelle, C., Balikhin, M., Dunlop, M., & Bauer, T. M. (2001). Kinetic study of the mirror mode. *Journal of Geophysical Research*, *106*(A10), 21611–21622. https://doi.org/10.1029/2000JA000457

Glassmeier, K. H., Motschmann, U., Mazelle, C., Neubauer, F. M., Sauer, K., Fuselier, S. A., & Acuña, M. H. (1993). Mirror modes and fast magnetoacoustic waves near the magnetic pileup boundary of comet P/Halley. *Journal of Geophysical Research*, *98*(A12), 20955–20964. https://doi.org/10.1029/93JA02582

Gosling, J. T., & Robson, A. E. (1985). Ion reflection, gyration, and dissipation at supercritical shocks. *Geophysical Monograph Series*, *35*, 141–152. https://doi.org/10.1029/GM035p0141

Halekas, J. S. (2017). Seasonal variability of the hydrogen exosphere of Mars. *Journal of Geophysical Research (Planets)*, *122*(5), 901–911. https://doi.org/10.1002/2017JE005306

Halekas, J. S., Brain, D. A., Luhmann, J. G., DiBraccio, G. A., Ruhunusiri, S., Harada, Y., et al. (2017a). Flows, fields, and forces in the mars-solar wind interaction. *Journal of Geophysical Research: Space Physics*, *122*(11), 11320–11341. https://doi.org/10.1002/2017JA024772

Halekas, J. S., Lillis, R. J., Mitchell, D. L., Cravens, T. E., Mazelle, C., Connerney, J. E. P., et al. (2015). MAVEN observations of solar wind hydrogen deposition in the atmosphere of Mars. *Geophysical Research Letters*, *42*(21), 8901–8909. https://doi.org/10.1002/2015GL064693

Halekas, J. S., & McFadden, J. P. (2021). Using solar wind helium to probe the structure and seasonal variability of the Martian hydrogen corona. *Journal of Geophysical Research (Planets)*, *126*(11), e07049. https://doi.org/10.1029/2021JE007049

Halekas, J. S., Ruhunusiri, S., Harada, Y., Collinson, G., Mitchell, D. L., Mazelle, C., et al. (2017b). Structure, dynamics, and seasonal variability of the mars-solar wind interaction: MAVEN solar wind ion analyzer in-flight performance and science results. *Journal of Geophysical Research: Space Physics*, *122*(1), 547–578. https://doi.org/10.1002/2016JA023167

Harada, Y., Ruhunusiri, S., Halekas, J. S., Espley, J., DiBraccio, G. A., Mcfadden, J. P., et al. (2019). Locally generated ULF waves in the Martian magnetosphere: MAVEN observations. *Journal of Geophysical Research: Space Physics*, *124*(11), 8707–8726. https://doi.org/10.1029/2019JA027312

Hasegawa, A. (1969). Drift mirror instability in the magnetosphere. *Physics of Fluids*, *12*(12), 2642–2650. https://doi.org/10.1063/1.1692407

Hellinger, P. (2007). Comment on the linear mirror instability near the threshold. *Physics of Plasmas*, *14*(8), 082105. https://doi.org/10.1063/1.2768318

Hellinger, P., Trávníček, P., Kasper, J. C., & Lazarus, A. J. (2006). Solar wind proton temperature anisotropy: Linear theory and wind/SWE observations. *Geophysical Research Letters*, *33*(9). https://doi.org/10.1029/2006GL025925

Horbury, T. S., & Lucek, E. A. (2009). Size, shape, and orientation of magnetosheath mirror mode structures. *Journal of Geophysical Research*, *114*(A5). https://doi.org/10.1029/2009JA014068

Huddleston, D. E., & Johnstone, A. D. (1992). Relationship between wave energy and free energy from pickup ions in the Comet Halley Environment. *Journal of Geophysical Research*, *97*(A8), 12217–12230. https://doi.org/10.1029/92JA00726

Huddleston, D. E., Strangeway, R. J., Blanco-Cano, X., Russell, C. T., Kivelson, M. G., & Khurana, K. K. (1999). Mirror-mode structures at the Galileo-Io flyby: Instability criterion and dispersion analysis. *Journal of Geophysical Research*, *104*(A8), 17479–17489. https://doi.org/10.1029/1999JA900195

Huddleston, D. E., Strangeway, R. J., Blanco-Cano, X., Russell, C. T., Kivelson, M. G., & Khurana, K. K. (2000). Io - Jupiter interaction: Waves generated by pickup ions. *Advances in Space Research*, *26*(10), 1513–1518. https://doi.org/10.1016/S0273-1177(00)00091-0

Jakosky, B. M., Lin, R. P., Grebowsky, J. M., Luhmann, J. G., Mitchell, D. F., Beutelschies, G., et al. (2015). The mars atmosphere and volatile evolution (MAVEN) mission. *Space Science Reviews*, *195*(1–4), 3–48. https://doi.org/10.1007/s11214-015-0139-x

Jarvinen, R., Alho, M., Kallio, E., & Pulkkinen, I. (2020a). Oxygen ion escape from Venus is modulated by ultra-low frequency waves. *Geophysical Research Letters*, *47*(11), e87462. https://doi.org/10.1029/2020GL087462

Jarvinen, R., Alho, M., Kallio, E., & Pulkkinen, T. I. (2020b). Ultra-low-frequency waves in the ion foreshock of Mercury: A global hybrid modelling study. *Monthly Notices of the Royal Astronomical Society*, *491*(3), 4147–4161. https://doi.org/10.1093/mnras/stz3257

Jarvinen, R., Kallio, E., & Pulkkinen, T. I. (2022). Ultra-low frequency foreshock waves and ion dynamics at mars. *Journal of Geophysical Research (Space Physics)*, *127*(5), e30078. https://doi.org/10.1029/2021JA030078

Jin, T., Lei, L., Yiteng, Z., Lianghai, X., & Fuhao, Q. (2022). Statistical analysis of the distribution and evolution of mirror structures in the Martian magnetosheath. *The Astrophysical Journal*, *929*(2), 165. https://doi.org/10.3847/1538-4357/ac5f00

Joy, S. P., Kivelson, M. G., Walker, R. J., Khurana, K. K., Russell, C. T., & Paterson, W. R. (2006). Mirror mode structures in the Jovian magnetosheath. *Journal of Geophysical Research*, *111*(A12), A12212. https://doi.org/10.1029/2006JA011985

Kivelson, M. G., & Southwood, D. J. (1996). Mirror instability II: The mechanism of nonlinear saturation. *Journal of Geophysical Research*, *101*(A8), 17365–17371. https://doi.org/10.1029/96JA01407

Kuznetsov, E. A., Passot, T., & Sulem, P. L. (2008). Nonlinear theory of mirror instability near its threshold. *JETP Letters*, *86*(10), 637–642. https://doi.org/10.1134/S0021364007220055

Lu, Q., Shan, L., Zhang, T., Zank, G. P., Yang, Z., Wu, M., et al. (2013). The role of pickup ions on the structure of the Venusian bow shock and its implications for the termination shock. *The Astrophysical Journal Letters*, *773*(2), L24. https://doi.org/10.1088/2041-8205/773/2/L24

Madanian, H., Halekas, J. S., Mazelle, C. X., Omidi, N., Espley, J. R., Mitchell, D. L., & McFadden, J. P. (2020). Magnetic holes upstream of the Martian bow shock: MAVEN observations. *Journal of Geophysical Research: Space Physics*, *125*(1). https://doi.org/10.1029/2019JA027198

Matteini, L., Hellinger, P., Landi, S., Trávníček, P. M., & Velli, M. (2012). Ion kinetics in the solar wind: Coupling global expansion to local microphysics. *Space Science Reviews*, *172*(1), 373–396. https://doi.org/10.1007/s11214-011-9774-z

Mazelle, C., Belmont, G., Glassmeier, K. H., Le Quéau, D., & Rème, H. (1991). Ultra low frequency waves at the magnetic pile-up boundary of comet P/Halley. *Advances in Space Research*, *11*(9), 73–77. https://doi.org/10.1016/0273-1177(91)90014-B

Mazelle, C., & Lembège, B. (2021). Evidence of the nonstationarity of the terrestrial bow shock from multi-spacecraft observations: Methodology, results, and quantitative comparison with particle-in-cell (PIC) simulations. *Annales Geophysicae*, *39*(4), 571–598. https://doi.org/10.5194/angeo-39-571-2021

Mazelle, C., Winterhalter, D., Sauer, K., Trotignon, J., Acuña, M., Baumgärtel, K., et al. (2004). Bow shock and upstream phenomena at mars. *Space Science Reviews*, *111*(1), 115–181. https://doi.org/10.1023/B:SPAC.0000032717.98679.d0

McFadden, J. P., Kortmann, O., Curtis, D., Dalton, G., Johnson, G., Abiad, R., et al. (2015). MAVEN SupraThermal and thermal ion compostion (STATIC) instrument. *Space Science Reviews*, *195*(1), 199–256. https://doi.org/10.1007/s11214-015-0175-6

Means, J. D. (1972). Use of the three-dimensional covariance matrix in analyzing the polarization properties of plane waves. *Journal of Geophysical Research*, *77*(28), 5551–5559. https://doi.org/10.1029/JA077i028p05551

Meziane, K., Mazelle, C., Wilber, M., Le Quéau, D., Eastwood, J., Rème, H., et al. (2004). Bow shock specularly reflected ions in the presence of low-frequency electromagnetic waves: A case study. *Annales Geophysicae*, *22*(7), 2325–2335. https://doi.org/10.5194/angeo-22-2325-2004

Mitchell, D. L., Mazelle, C., Sauvaud, J.-A., Thocaven, J.-J., Rouzaud, J., Fedorov, A., et al. (2016). The MAVEN solar wind electron analyzer. *Space Science Reviews*, *200*(1), 495–528. https://doi.org/10.1007/s11214-015-0232-1

Passot, T., Ruban, V., & Sulem, P. L. (2006). Fluid description of trains of stationary mirror structures in a magnetized plasma. *Physics of Plasmas*, *13*(10), 102310. https://doi.org/10.1063/1.2356485

Passot, T., & Sulem, P. L. (2008). Stability and formation of mirror structures: A fluid approach. *Communications in Nonlinear Science and Numerical Simulation*, *13*(1), 141–146. https://doi.org/10.1016/j.cnsns.2007.04.001

Pokhotelov, O. A., Onishchenko, O. G., Balikhin, M. A., Treumann, R. A., & Pavlenko, V. P. (2001). Drift mirror instability in space plasmas, 2, Nonzero electron temperature effects. *Journal of Geophysical Research*, *106*(A7), 13237–13246. https://doi.org/10.1029/2000JA000310

Pokhotelov, O. A., Sagdeev, R. Z., Balikhin, M. A., & Treumann, R. A. (2004). Mirror instability at finite ion-Larmor radius wavelengths. *Journal of Geophysical Research*, *109*(A9). https://doi.org/10.1029/2004JA010568

Price, C. P. (1989). Mirror waves driven by newborn ion distributions. *Journal of Geophysical Research*, *94*(A11), 15001–15009. https://doi.org/10.1029/JA094iA11p15001

Price, C. P., Swift, D. W., & Lee, L.-C. (1986). Numerical simulation of nonoscillatory mirror waves at the Earth's magnetosheath. *Journal of Geophysical Research*, *91*(A1), 101–112. https://doi.org/10.1029/JA091iA01p00101

Rahmati, A., Larson, D. E., Cravens, T. E., Lillis, R. J., Halekas, J. S., McFadden, J. P., et al. (2017). MAVEN measured oxygen and hydrogen pickup ions: Probing the Martian exosphere and neutral escape. *Journal of Geophysical Research (Space Physics)*, *122*(3), 3689–3706. https://doi.org/10.1002/2016JA023371

Romanelli, N., Bertucci, C., Gómez, D., Mazelle, C., & Delva, M. (2013). Proton cyclotron waves upstream from mars: Observations from mars global surveyor. *Planetary and Space Science*, *76*, 1–9. https://doi.org/10.1016/j.pss.2012.10.011

Romanelli, N., Mazelle, C., Chaufray, J. Y., Meziane, K., Shan, L., Ruhunusiri, S., et al. (2016). Proton cyclotron waves occurrence rate upstream from Mars observed by MAVEN: Associated variability of the Martian upper atmosphere. *Journal of Geophysical Research (Space Physics)*, *121*(11), 11–113. https://doi.org/10.1002/2016JA023270

Romeo, O. M., Romanelli, N., Espley, J. R., Mazelle, C., DiBraccio, G. A., Gruesbeck, J. R., & Halekas, J. S. (2021). Variability of upstream proton cyclotron wave properties and occurrence at mars observed by MAVEN. *Journal of Geophysical Research (Space Physics)*, *126*(2), e28616. https://doi.org/10.1029/2020JA028616

Ruhunusiri, S., Halekas, J. S., Connerney, J. E. P., Espley, J. R., McFadden, J. P., Larson, D. E., et al. (2015). Low-frequency waves in the Martian magnetosphere and their response to upstream solar wind driving conditions. *Geophysical Research Letters*, *42*(21), 8917–8924. https://doi.org/10.1002/2015GL064968

Russell, C. T., Huddleston, D. E., Strangeway, R. J., Blanco-Cano, X., Kivelson, M. G., Khurana, K. K., et al. (1999). Mirror-mode structures at the Galileo-Io Flyby: Observations. *Journal of Geophysical Research*, *104*(A8), 17471–17478. https://doi.org/10.1029/1999JA900202

Russell, C. T., Jian, L. K., Luhmann, J. G., Zhang, T. L., Neubauer, F. M., Skoug, R. M., et al. (2008). Mirror mode waves: Messengers from the coronal heating region. *Geophysical Research Letters*, *35*(15). https://doi.org/10.1029/2008GL034096

Samson, J. C., & Olson, J. V. (1980). Some comments on the descriptions of the polarization states of waves. *Geophysical Journal*, *61*(1), 115–129. https://doi.org/10.1111/j.1365-246X.1980.tb04308.x

Simon Wedlund, C., Volwerk, M., Beth, A., Mazelle, C., Möstl, C., Halekas, J., et al. (2022). A fast bow shock location predictor-estimator from 2D and 3D analytical models: Application to mars and the maven mission. *Journal of Geophysical Research: Space Physics*, *127*(1), e2021JA029942. https://doi.org/10.1029/2021JA029942

Simon Wedlund, C., Volwerk, M., Beth, A., Mazelle, C., Möstl, C., Halekas, J., et al. (2021). Predicted times, spatial coordinates of bow shock crossings and shock geometry at Mars from the NASA/MAVEN mission, using spacecraft ephemerides and magnetic field data, with a predictor-corrector algorithm. *Zenodo*. https://doi.org/10.5281/zenodo.6320518

Simon Wedlund, C., Volwerk, M., Mazelle, C., Halekas, J., Rojas-Castillo, D., Espley, J., & Möstl, C. (2022). Making waves: Mirror mode structures around mars observed by the maven spacecraft. *Journal of Geophysical Research: Space Physics*, *127*(1), e2021JA029811. https://doi.org/10.1029/2021JA029811

Simon Wedlund, C., Volwerk, M., Mazelle, C., Rojas Mata, S., Stenberg Wieser, G., Futaana, Y., et al. (2023). Statistical distribution of mirror-mode-like structures in the magnetosheaths of unmagnetised planets – Part 1: Mars as observed by the maven spacecraft. *Annales Geophysicae*, *41*(1), 225–251. https://doi.org/10.5194/angeo-41-225-2023

Slavin, J. A., & Holzer, R. E. (1981). Solar wind flow about the terrestrial planets 1. Modeling bow shock position and shape. *Journal of Geophysical Research*, *86*(A13), 11401–11418. https://doi.org/10.1029/JA086iA13p11401

Soucek, J., & Escoubet, C. P. (2011). Cluster observations of trapped ions interacting with magnetosheath mirror modes. *Annals of Geophysics*, *29*(6), 1049–1060. https://doi.org/10.5194/angeo-29-1049-2011

Soucek, J., Lucek, E., & Dandouras, I. (2008). Properties of magnetosheath mirror modes observed by Cluster and their response to changes in plasma parameters. *Journal of Geophysical Research*, *113*(A4). https://doi.org/10.1029/2007JA012649

Szegö, K., Glassmeier, K.-H., Bingham, R., Bogdanov, A., Fischer, C., Haerendel, G., et al. (2000). Physics of mass loaded plasmas. *Space Science Reviews*, *94*, 429–671. https://doi.org/10.1023/A:1026568530975

Tsurutani, B. T., Echer, E., Verkhoglyadova, O. P., Lakhina, G. S., & Guarnieri, F. L. (2011). Mirror instability upstream of the Termination Shock (TS) and in the heliosheath. *Journal of Atmospheric and Solar-Terrestrial Physics*, *73*(11), 1398–1404. https://doi.org/10.1016/j.jastp.2010.06.007

Tsurutani, B. T., Lakhina, G. S., Verkhoglyadova, O. P., Echer, E., Guarnieri, F. L., Narita, Y., & Constantinescu, D. O. (2011). Magnetosheath and heliosheath mirror mode structures, interplanetary magnetic decreases, and linear magnetic decreases: Differences and distinguishing features: Review. *Journal of Geophysical Research*, *116*(A2). https://doi.org/10.1029/2010JA015913

Tsurutani, B. T., & Smith, E. J. (1986). Strong hydromagnetic turbulence associated with comet giacobini-zinner. *Geophysical Research Letters*, *13*(3), 259–262. https://doi.org/10.1029/GL013i003p00259

Vedenov, A. A., & Sagdeev, R. Z. (1961). Some properties of a plasma with an anisotropic ion velocity distribution in a magnetic field. *Plasma Physics and the Problem of Controlled Thermonuclear Reactions*, *3*, 332. http://adsabs.harvard.edu/abs/1961ppp3.conf..332V

Verigin, M. I., Tátrallyay, M., Erdős, G., & Kotova, G. A. (2006). Magnetosheath Interplanetary medium reference frame: Application for a statistical study of mirror type waves in the terrestrial plasma environment. *Advances in Space Research*, *37*(3), 515–521. https://doi.org/10.1016/j.asr.2005.03.042

Verscharen, D., Klein, K. G., & Maruca, B. A. (2019). The multi-scale nature of the solar wind. *Living Reviews in Solar Physics*, *16*(1), 5. https://doi.org/10.1007/s41116-019-0021-0

Wang, J., Lee, L. C., Xu, X., Cao, J. B., Yu, J., Chang, Q., et al. (2020). Plasma and magnetic-field structures near the Martian induced magnetosphere boundary. I. Plasma depletion region and tangential discontinuity. *A&*, *642*, A34. https://doi.org/10.1051/0004-6361/201936201

Yamauchi, M., Hara, T., Lundin, R., Dubinin, E., Fedorov, A., Sauvaud, J. A., et al. (2015). Seasonal variation of Martian pick-up ions: Evidence of breathing exosphere. *Planetary and Space Science*, *119*, 54–61. https://doi.org/10.1016/j.pss.2015.09.013